AN ABSTRACT OF THE THESIS OF

CHARLES WILLIAM ROGERS (Name) for the DOCTOR OF PHILOSOPHY (Degree)

in PHYSICS (Major) presented on 8/16/71 (Date)

Title: INELASTIC SCATTERING OF 17-MeV PROTONS FROM ^{14}N AND ^{15}N

Redacted for Privacy

Abstract approved: Peter Fessenden

An inelastic scattering experiment was done in which 17-MeV protons from the Oregon State University cyclotron were scattered from ^{14}N and ^{15}N gas targets. Angular distributions are shown for the ground, 6.32-, 7.56-, 8.31-, and 8.57-MeV states and the 5.3- and 7.2-MeV unresolved doublets of ^{15}N, and for the ground, 2.3-, 3.9-, 6.2-, 6.4-, and 7.0-MeV states and the 5-, 5.7-, 8-, and 8.5-MeV unresolved doublets of ^{14}N. Reasonable fits to the data were obtained for the 6.32-MeV ^{15}N state and the 2.3- and 3.9-MeV ^{14}N states using a microscopic potential in a coupled-channel calculation. The use of a tensor force improved the fits to both the 6.32-MeV ^{15}N state and the 2.3-MeV ^{14}N state.

A weak-coupling model was considered in which excited ^{15}N states are formed by coupling a $p_{1/2}$ proton hole to excited states of ^{16}O. The model adequately represents the 5.27- and 7.56-MeV ^{15}N

states as being formed from the 6.13-MeV ^{16}O state, and the 5.30- and 7.30-MeV ^{15}N states as being formed from the 7.12-MeV ^{16}O state. The 6.32-MeV ^{15}N state does not seem to be related to the 6.92-MeV ^{16}O state, but evidence was presented that the 9.16-MeV ^{15}N state is related by the weak-coupling model to the 6.92-MeV ^{16}O state.

Inelastic Scattering of 17-MeV Protons from ^{14}N and ^{15}N

by

Charles William Rogers

A THESIS

submitted to

Oregon State University

in partial fulfillment of
the requirements for the
degree of

Doctor of Philosophy

June 1972

APPROVED;

Redacted for Privacy

Assistant Professor of Physics

in charge of major

Redacted for Privacy

Chairman of Department of Physics

Redacted for Privacy

Dean of Graduate School

Date thesis is presented 8/16/71

Typed by Clover Redfern for Charles William Rogers

ACKNOWLEDGMENT

Thanks are due to Dr. C. Zafiratos whose initial suggestion led to the experiment described herein.

Special thanks go to J. Archibald, J. McKenzie, and Dr. M. Wilson for their work in preparing and operating the Oregon State University cyclotron, and to M. Stomp and Dr. F. Schmittroth for their coupled-channel program and assistance in using it.

Thanks are expressed to Dr. M. Cutler and Dr. L. Schecter for their assistance in the preparation of this thesis.

Special thanks are given to Dr. V. Madsen for his invaluable assistance with the theory and to Dr. P. Fessenden for his careful guidance throughout the experiment and the preparation of this thesis.

A final special note of thanks goes to my wife, JoAnne, for her understanding and patience during the performance of the experiment and preparation of this thesis.

TABLE OF CONTENTS

LIST OF TABLES

LIST OF FIGURES

INELASTIC SCATTERING OF 17-MeV PROTONS FROM ^{14}N AND ^{15}N

I. INTRODUCTION

A basic goal in nuclear physics is to understand the nuclear force. A major step in this direction is taken by the formulation of a microscopic model which attempts to describe directly measurable quantities (e.g., reaction differential cross sections) in terms of nuclear structure and an assumed form of the nucleon-nucleon interaction. The microscopic model employed in the present work is that of Madsen (29), which, although still in a state of development (e.g., should spin-orbit effects or exchange contributions be included (3, 5, 6, 36)), has enjoyed considerable success (4, 7, 36, 46, 59).

The interpretation of the (p, p') reaction in terms of the microscopic model is expected to be more straightforward than for a reaction involving a complex projectile (e.g., (d, d')). When using a complex projectile the effect of each nucleon of the projectile must be averaged and an effective two-body potential obtained.

It was decided to investigate the $^{14}N(p, p')^{14}N$ and the $^{15}N(p, p')^{15}N$ reactions because of the theoretical interest in the low lying states of the nitrogen isotopes and because of the experimental feasibility. The states of interest are well enough separated in energy and have high enough yields to be resolved and measured by

the experimental apparatus available. In order to minimize effects due to background reactions, it was decided to construct and use a gas target for both the ^{14}N and ^{15}N work. (Nitrogen gas enriched to 99% $^{15}N_2$ is available commercially.)

The 2.3-MeV, 0^+ state of ^{14}N holds considerable interest because a tensor component must be included in the nuclear force in order to explain existing experimental data (12, 40, 46, 47, 55, 60). The references cited establish the necessity of a tensor force and give a preliminary value of its magnitude. It is of interest to further investigate the tensor force by applying the model to the reaction $^{14}N(p, p')^{14}N$ (2.3-MeV state) with the 17-MeV protons and improved accuracy of the present experiment. It is also of interest to investigate the role of the tensor force in the $^{15}N(p, p')^{15}N$ reaction, since a weak-coupling model has been proposed in which some low-lying states of ^{15}N are formed from the low-lying states of ^{14}N (including the 2.3-MeV state) (37).

The low-lying states of ^{15}N have received considerable attention (2, 7, 10, 17-23, 26, 28, 32, 37, 41-43, 45, 48, 49, 52, 56, 58). Since ^{15}N can be thought of as a single proton hole in an otherwise closed shell, one hopes that the structure of its states is simple and straightforward. The low-lying positive-parity states of ^{15}N have been described by coupling a proton hole to excited states of ^{16}O or a neutron to excited states of ^{14}N in a weak-coupling model (10, 37).

A similar model was unsuccessfully attempted for the negative-parity states of ^{15}N (see, e.g., 42). Some evidence indicates that the lowest negative-parity states (ground state and 6.3-MeV state) are mainly single-particle, simple shell-model states. That this is an oversimplification is apparent from the fact that this simple approach cannot explain the observed electromagnetic transition rates (see, e.g., 18, 32, 42, 48). It is therefore of interest to investigate the $^{15}N(p, p')^{15}N$ reaction, extracting differential cross sections for the excited states (only ground state cross sections have previously been measured for this reaction). One would hope then, by analyzing the results with the microscopic model, to learn more about the ^{15}N structure.

II. EXPERIMENT

Proton Beam

The proton beam is from the Oregon State University 37-inch isochronous cyclotron. A negative ion beam (H^-) is accelerated in the cyclotron until it reaches a thin aluminum stripper foil located between one of the dees and 17 inches from the cyclotron center. As an H^- ion passes through the stripper foil it loses both its electrons. The resulting H^+ ion (p) reverses its curvature and is deflected outside the main magnetic field and into an external beam handling system. Energy analysis is accomplished with an 80 degree bending magnet and a pair of vertical tantalum slits (spaced 0.1 inches apart) set at its focus. The beam is then focused by a quadrupole lens pair to form a beam spot approximately 0.1 inches square at the target position. (A spot formed by exposing a glass slide with the beam measured 0.08 inches wide by 0.13 inches high.)

A beam intensity of from 10 to 15 nanoamperes was used; the beam being collected in a Faraday cup and measured with a current integrator. The beam was also monitored by observing the elastic scattering peak in a detector placed at a fixed forward angle (usually about 20 degrees). The time for a run varied from a few minutes at forward angles to more than an hour at other angles.

Data taken at the same angle, but on different days, agreed

within the experimental error. This indicated that the system was stable so that making long runs, or collecting data over several days, did not increase the experimental error.

The beam energy (before correction for energy loss in the target) was determined to be 17.46 ± 0.15 MeV. A polyethelene target and the kinematical crossover technique described by Smythe (51) were used for this determination.

The overall energy resolution of the system was measured to be 105 keV by looking at protons elastically scattered from Au at forward angles. The target was a single layer of gold leaf, and was thin enough so that it contributed negligible energy spread.

Electronics and Detector

Protons were scattered from ^{14}N and ^{15}N and were observed with a solid state detector. Modular solid state electronics were employed; Figure 1 is a schematic of the electronics setup. The single channel analyzer in the monitor line was set such that only elastic scattering events were counted by the scaler. The single channel analyzer and linear gate in the primary detector line were used to prevent low voltage signals (noise and detector pulses from protons inelastically scattered from unresolved, highly excited target states) from entering the 512-channel analyzer and increasing its dead time. Whenever the analyzer dead time could not be neglected, a

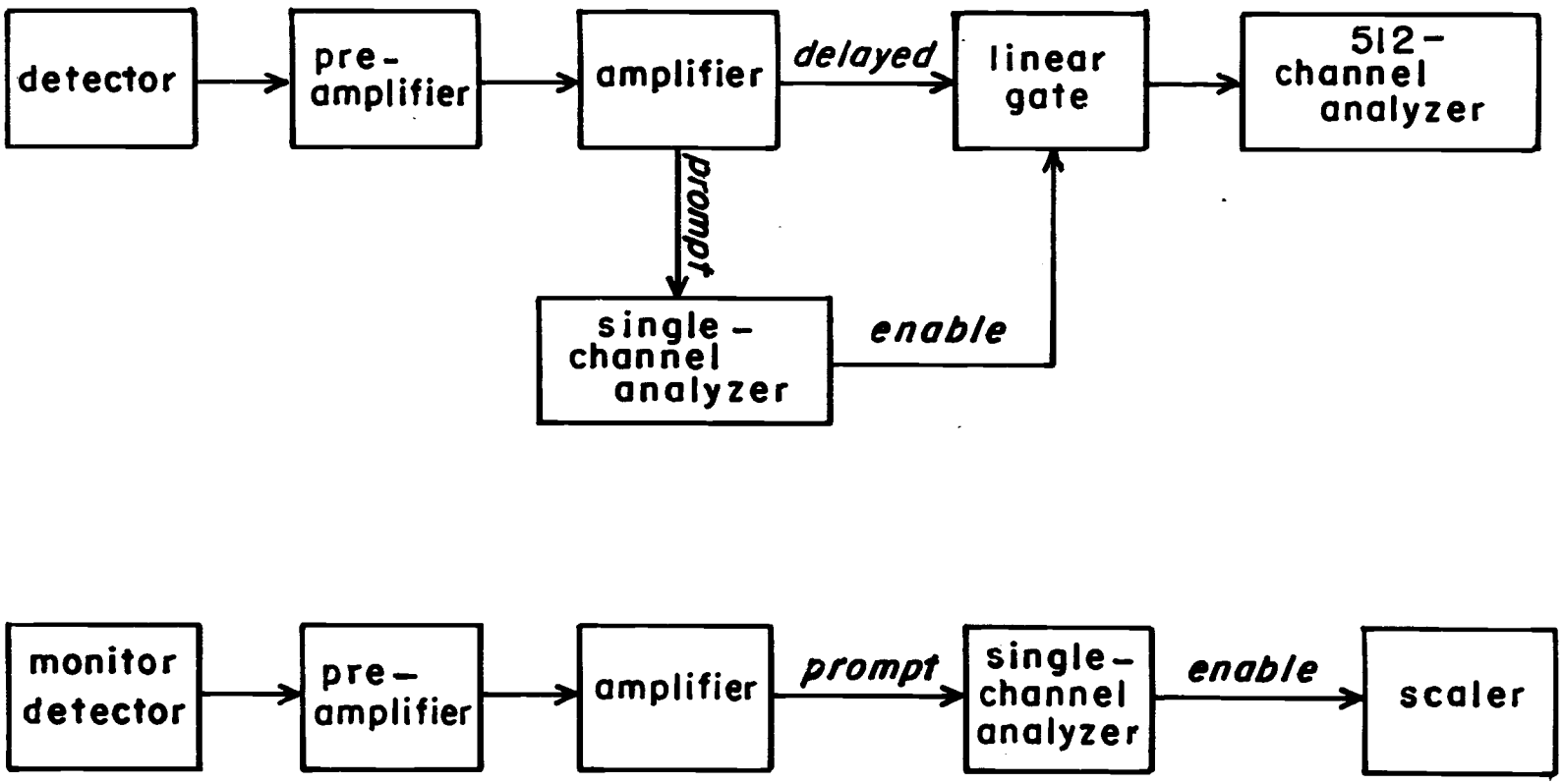

Figure 1. Detector electronics.

correction was made by multiplying the charge collected in the Faraday cup by the ratio of analyzer live time divided by the elapsed real time for the run.

The primary detector employed was a Kevex[1] lithium drifted detector having an active area of 110 square millimeters and an active depth (with full bias voltage) of three millimeters.

Electronics for a particle identification system were available but not used because a large area, sufficiently thin ΔE counter was not available. Preliminary runs on the nitrogen isotopes did not reveal any appreciable non-proton events, but subsequent analysis did reveal the occurrence of the $^{15}N(p,\alpha)^{12}C$ reaction at some angles. The alpha peaks were identified by their kinematic shift with reaction angle. Their contribution was then subtracted from the proton spectra.

The gas target volume viewed by the detector was defined by a set of collimating slits (Figure 2). One tantalum slit, 1/16 inch wide by 0.28 inches high, was placed 2.75 centimeters from the target center, while a second slit, 1/16 inch wide by 7/16 inches high, was placed at the detector (16.5 centimeters from the target center). In order to keep beam from striking it, the first slit was placed at 8 centimeters from the target center when viewing reactions making an

[1] Kevex corp., 898 Mahler Road, Burlingame, Calif.

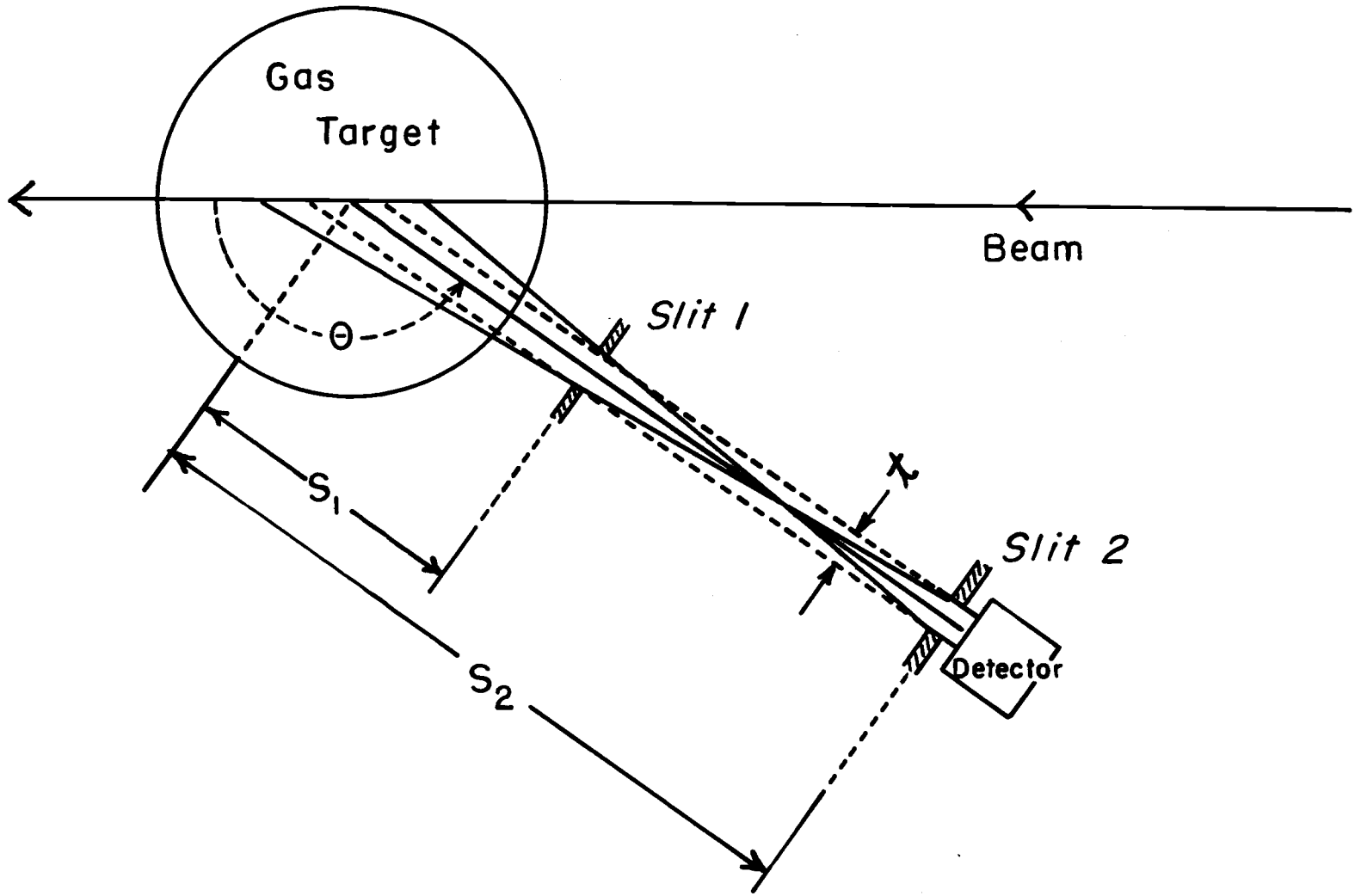

Figure 2. Scattering geometry.

angle of 25 degrees or less with the beam.

The angular resolution is given by

$$\Delta\theta = \frac{W}{S_2}\left(\frac{2S_2}{S_2 - S_1}\right). \qquad (1)$$

S_1 is the distance from the target center to the first slit, and S_2 is the distance from the target center to the slit at the detector. W is the width of either slit. The factor in parentheses results because reactions can scatter protons into the detector from locations in the gas other than only directly in front of the slits (as is the usual case for a thin target). The result was $\Delta\theta \simeq 1.3$ degrees, for $S_1 = 2.75$ centimeters, $W = 1/16$ inch, and $S_2 = 16.5$ centimeters; while for $S_1 = 8$ centimeters (W and S_2 remaining fixed), $\Delta\theta \simeq 2.0$ degrees.

Targets

A gas target was used to avoid background from protons interactiong with elements other than nitrogen. Gas enriched to 99% $^{15}N_2$ was commercially available.[2]

The target cell (Figure 3) was based on the design of Mollenauer (30). As viewed from the center, each of the four posts of the cell

[2] BIO-RAD Laboratories, 32nd and Griffin Avenus, Richmond, Calif.

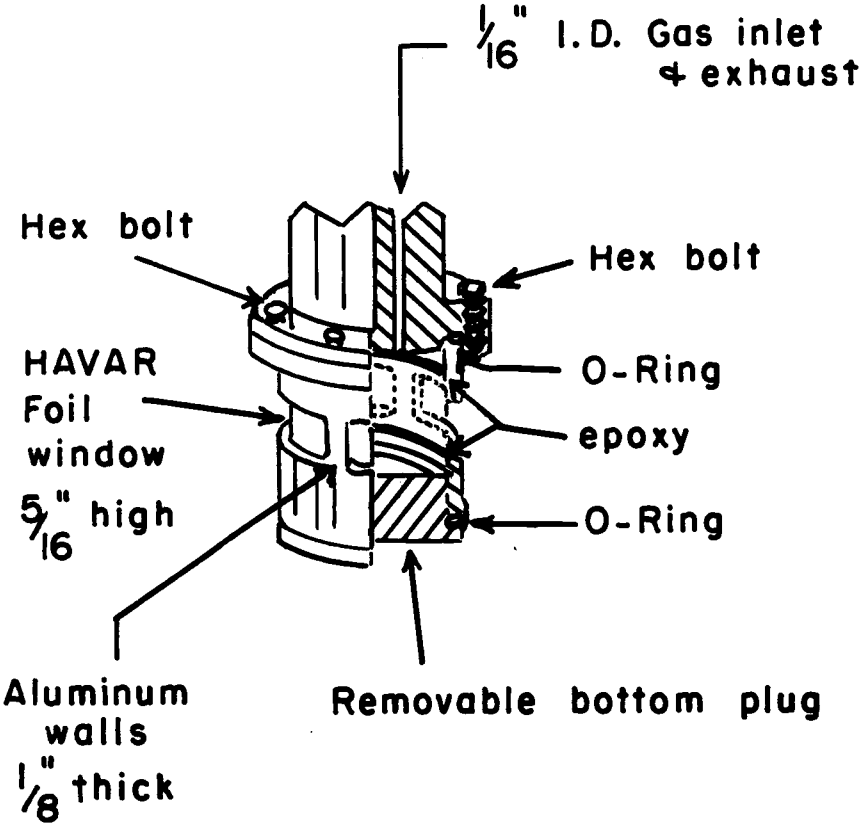

Figure 3. Gas target.

subtends an angle of about 16 degrees, while each of the four windows subtends about 74 degrees. Every effort was made to minimize the internal volume of the target in order to minimize the amount of target gas necessary. The windows were of Havar foil[3] 0.00016 inches thick. It was found that great care had to be used in preparing the cell and putting in the windows. Edges in contact with the foil had to be carefully rounded. Then the cell was slightly heated and epoxy applied around the inside rims of the cell. Next the foil was put into place and epoxy placed around the edges and the overlap seam (behind a post). The cell was again slightly heated to make the epoxy flow a little. Cells prepared in this fashion were tested successfully at positive pressures ranging up to seven atmospheres.

The gas cell was attached to a shaft which passed through a sliding seal in a flange. The flange was bolted to the top of a 17 inch Ortec scattering chamber.[4] A valve and pressure gauge mounted on top of the shaft communicated with the gas cell through a 1/16 inch diameter stainless steel tube. The gauge allowed the pressure to be monitored continuously. The gas target cell could be lowered into the beam line and rotated. The design shown in Figure 3 allowed reactions to be observed at any scattering angle.

---

[3] Hamilton Watch Co., Precision Metals Division, Lancaster, Penn.

[4] Oak Ridge Technical Enterprises Corp., Oak Ridge, Tenn.

Gas Handling System

The ^{15}N was supplied in glass ampules at slightly below one atmosphere pressure. A special gas handling system (Figure 4) was built to extract the gas from the ampules and to insert it into the target cell at an increased pressure.

Since the cell windows could not sustain a negative pressure, the space around the target cell was first evacuated. Next, the rest of the gas handling system and interior of the target cell was brought to a high vacuum. Gas was transferred from the ampule to the ballast tank by pumping on liquid nitrogen surrounding the ballast tank. The rapid evaporation of the liquid nitrogen cooled the ballast tank sufficiently to draw the nitrogen gas from the ampule into the ballast tank where it condensed as a liquid. Gas was driven into the target cell by closing the valve to the ampule and heating the ballast tank.

The system proved to be more efficient if, after the first ballast tank was filled, it was replaced by a second tank of larger volume. Gas was again withdrawn from the ampule by cooling the second ballast tank. The second tank was sealed and removed. The first tank was then placed in the liquid nitrogen; the second was connected to it and heated, driving more ^{15}N into the first ballast tank. The volume of the first ballast tank and of the gas lines to the target cell were minimized in order to conserve gas. Using the method outlined above,

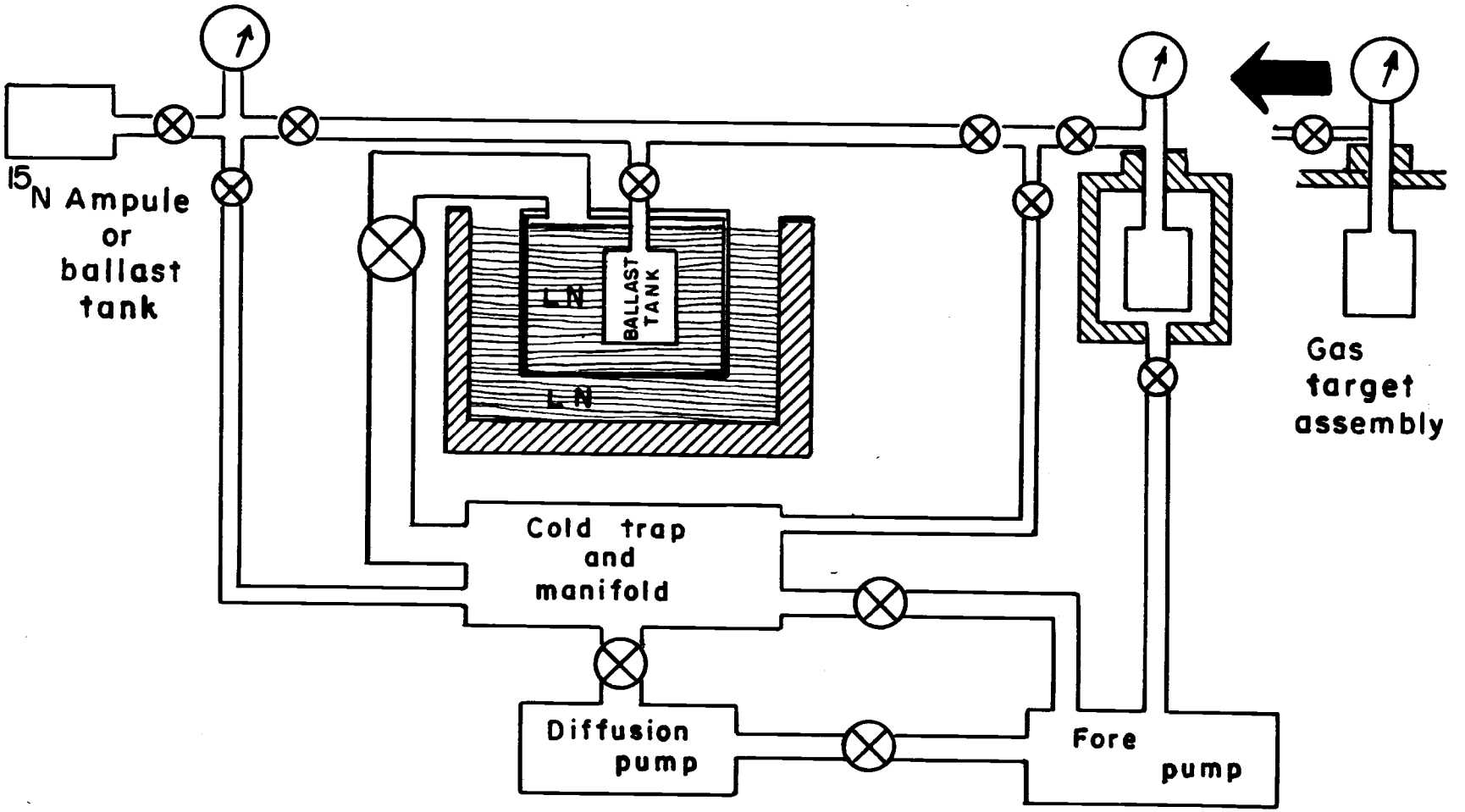

Figure 4. Gas handling system.

gas from two 100 cubic centimeter ampules was sufficient to pressurize the gas cell at from two to three atmospheres.

Data Reduction

Since the detector subtended a finite solid angle, the differential scattering cross section, $\frac{d\sigma(\theta)}{d\Omega}$, is approximated by $\frac{\Delta\sigma(\theta)}{\Delta\Omega}$. The laboratory cross section is related to measurable quantities by

$$\frac{\Delta\sigma(\theta)}{\Delta\Omega} = 2.54 \times 10^{-29} \frac{cm^2 N \sin(\theta) T}{aQPW\Delta\Omega g} . \qquad (2)$$

N = number of scattered protons detected,

θ = laboratory scattering angle (refer to Figure 2),

a = number of target atoms/molecule,

Q = total integrated beam in microcoulombs,

T = temperature in degrees Kelvin,

P = absolute target pressure in lbs/in^2,

W = slit width in centimeters,

$\Delta\Omega$ = solid angle subtended by the detector, and

g = a correction factor due to the extended nature of the target.

To zeroth order, $g = \frac{S_2}{S_2 - S_1}$. Higher order corrections to g are discussed by Silverstein (50). Applying these higher order corrections to the present experiment showed that they were negligible (a few tenths of one percent).

The proton beam diverges within the target due to multiple scattering in the gas and foil. The effect of this divergence upon the cross section was estimated by adapting the results of Critchfield and Dodder (11) to the present case. The estimate showed this correction to be less than one percent in general, but it could be as large as several percent at an angle of ten degrees or less from the beam line, the worst possible case. Due to the uncertainty in the estimates, no correction was made to the cross section; rather, the overall experimental uncertainty was increased slightly except at small angles from the beam line. At such angles no attempt was made to reflect the uncertainty due to beam divergence, since there are other factors which may contribute large uncertainties (see below).

The energy lost by the proton beam in traversing the target was not negligible. In traveling through the foil window and to the target center, the beam lost about 270 keV in the ^{14}N target used (73.7 lbs/in^2) and about 170 keV in the ^{15}N target (34.4 lbs/in^2). The energy resolution of the scattered protons is a function of apparent target thickness, which itself is a function of the scattering angle. The overall energy resolution is generally a slowly varying function of the scattering angle because the contribution due to straggling in the target is in addition to the energy spread of the beam (before it reaches the target). The overall energy resolution was typically about 200 keV full width at half maximum (FWHM) for the ^{14}N target

(160 keV for the ^{15}N target) except at scattering angles beyond 160 degrees. At such large scattering angles the straggling in the target completely dominated, and the energy resolution deteriorated to 300-400 keV.

Considering this problem further, for $\theta \lesssim 20°$ and $\theta \gtrsim 160°$, reactions which take place throughout a full diameter of the target can scatter protons into the detector. This results in an energy-averaged cross section being measured from those angles. In the worst possible case (the ^{14}N target and θ such that reactions from the front to the back of the target are observed), reactions are observed from 17.4 MeV (on the average) at the leading edge of the target to 17.0 MeV at the far edge of the target. Hence, if the cross section being measured changes rapidly with energy, the measurement may be in error at these extreme angles.

In order to check the experimental apparatus, the correction estimates, and the data reduction method, elastic and inelastic scattering of protons from ^{12}C were measured using a CO_2 target at 34 lbs/in^2 pressure. The ground state data (Figure 5) were taken at 17.1 ± 0.15 MeV and extend from 65 degrees to 170 degrees. The present data are compared with data from Daehnick and Sherr (15) taken at 17.0 ± 0.15 MeV with a thin carbon foil target. From 65 degrees to 135 degrees the two curves differ at most by 15%; beyond 135 degrees the difference increases to about 25%. As an indication

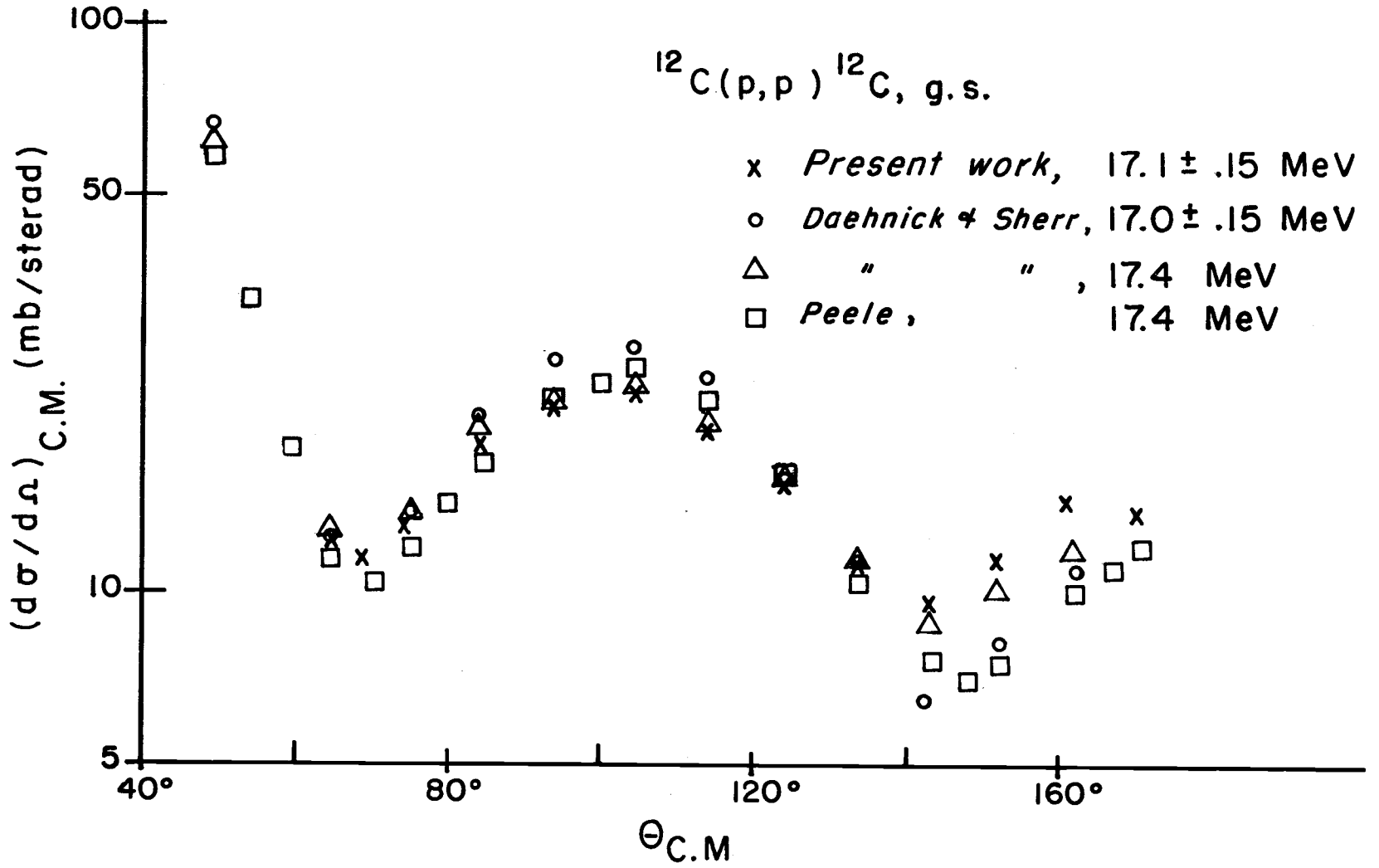

Figure 5. Angular distribution for the $^{12}C(p,p)^{12}C$, ground state, reaction. The total experimental error is about 5% in all cases; Daehnick and Sherr (15), Peele (34).

that this difference is not necessarily the result of the gas target or other aspects of the present experiment, it is noted that data for the ground state of carbon at an incoming proton energy of 17.4 MeV as given by Daehnick and Sherr (15) show a similar difference when compared with the 17.4 MeV data of Peele (34). Peele does not give data near 17.1 MeV. The first excited state of the present experiment and that of Daehnick and Sherr (15) are in excellent agreement, differing by 10% or less except for angles less than 30 degrees (see Figure 6).

As a further check of the experimental system and method of analysis, cross sections with CO_2 in the gas target were measured from 30 degrees to 160 degrees and at several different pressures. It was found that the data agreed to within experimental error, except when large pressure differences (50%) were involved for measurements at extreme angles.

These checks indicate that data taken with the present method are valid to within the experimental error quoted, except for $\theta \lesssim 25°$ and $\theta \gtrsim 160°$.

The experimental error for the intermediate angles was, in general, 10% or less. The total error due to uncertainty in pressure, temperature, charge collected, slit width, and slit position was estimated to be less than 6%. Errors due to counting statistics and uncertainty in background subtraction were generally negligible for the ground state, and 5% or less for the excited states (except as shown).

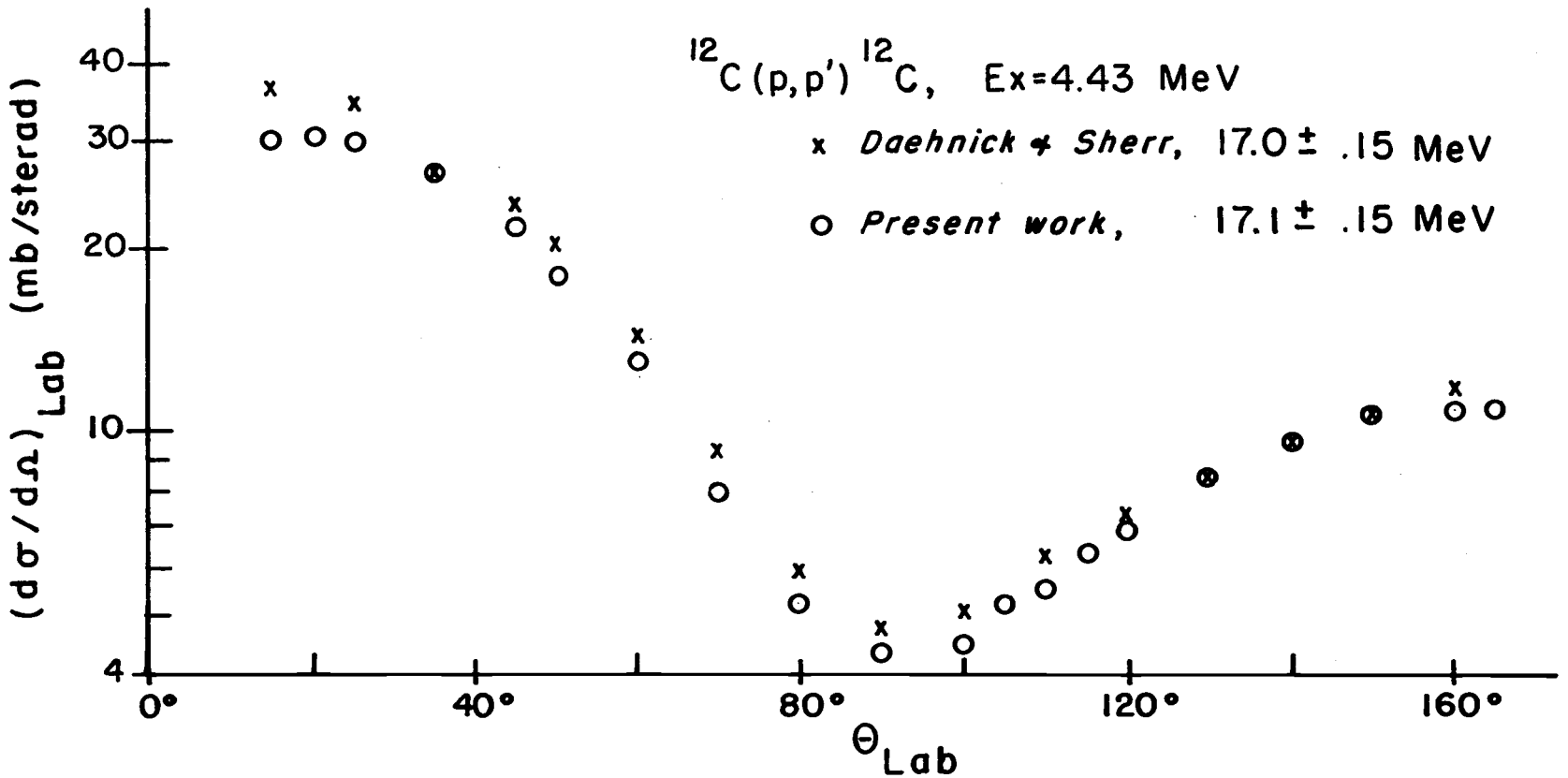

Figure 6. Angular distribution for the $^{12}C(p,p')^{12}C$, 4.43-MeV state, reaction. The total experimental error is about 6% in all cases; Daehnick and Sherr (15).

The error bars shown on the experimental data represent the error due to all causes, except that no attempt has been made to reflect the uncertainties due to energy averaging of the cross sections or beam divergence effects at extreme angles.

Target impurities were identified by the energy of the impurity peak and its variation with scattering angle (see Figures 8 and 9). The magnitude of the impurity peak is a measure of the amount of impurity present. On this basis it was determined that the ^{15}N target contained $5.0 \pm 1.5\%$ ^{14}N, while the ^{14}N target contained $1.6 \pm 0.2\%$ ^{16}O and $1.6 \pm 0.2\%$ ^{12}C. Impurity contributions to the target state cross sections were removed by subtracting the above percentages multiplied by the impurity state cross sections from the measured target state cross sections. The ^{14}N cross sections of the present work, the ^{12}C cross sections of Daehnick and Sherr (15), and the ^{16}O cross sections of Crawley and Garvey (13) were used for the impurity subtractions.

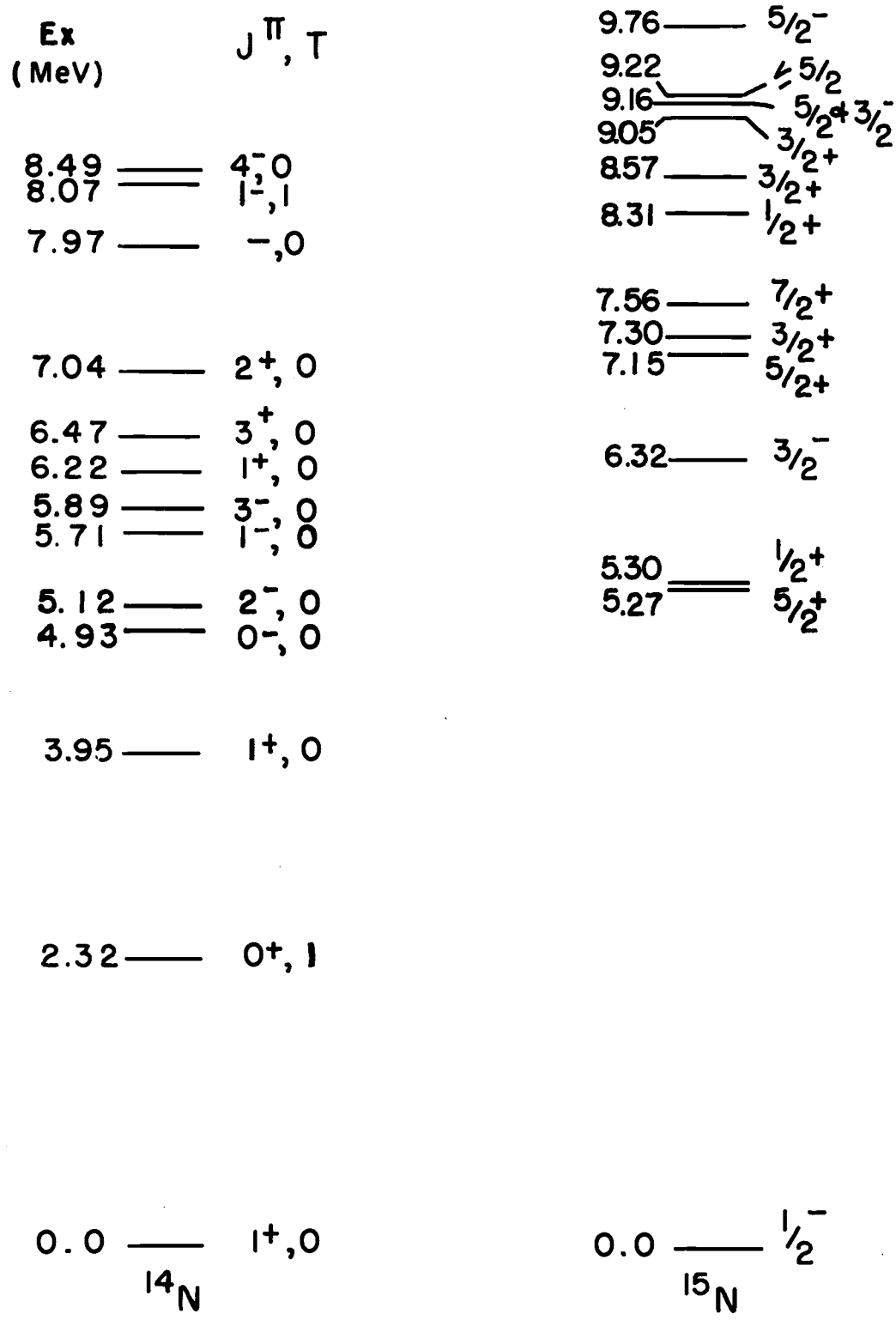

Figure 7. Energy levels of ^{14}N (reference 24) and ^{15}N (reference 49).

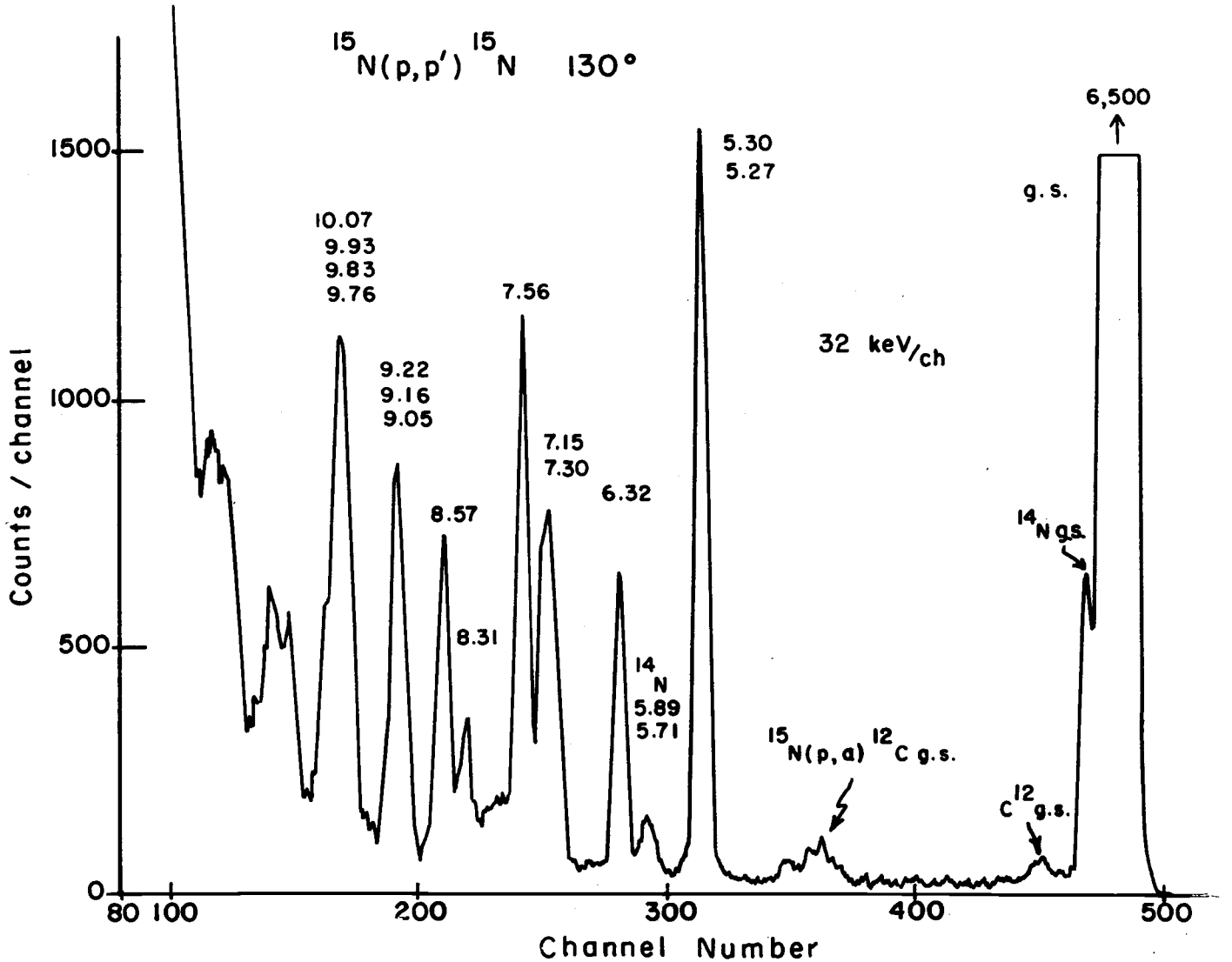

Figure 8. Proton energy spectrum for ^{15}N. The states are identified by their excitation energy in MeV.

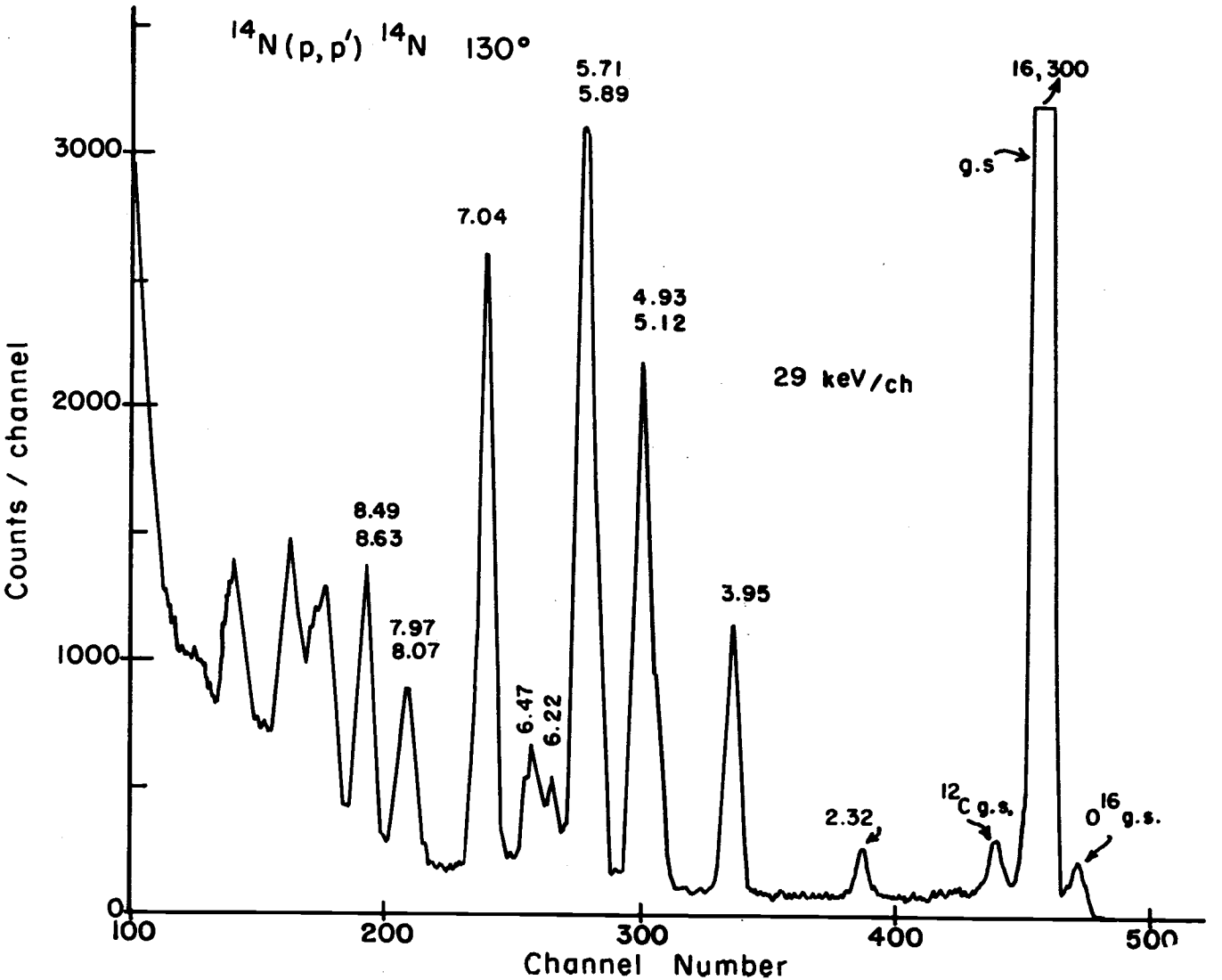

Figure 9. Proton energy spectrum for ^{14}N. The states are identified by their excitation energy in MeV.

III. THEORY

Introduction

Several formalisms have been presented to describe nuclear reactions. Two of the more successful and generally used formalisms are the distorted-wave Born approximation (DWBA) (see, e.g., 44) and the coupled-channel calculation (CC-calculation) (see, e.g., 54). In DWBA the cross section is calculated in a perturbation-theory approach. Usually only the first order term is calculated, as the higher order terms become increasingly difficult to calculate. Hence DWBA is expected to be most accurate when the interaction which causes the nuclear reaction is weak.

The CC-calculation treats the interaction exactly, although it restricts the number of channels considered (six for the computer code used in this work). If all the channels which strongly couple can be included, the approximation is very good even for strong interactions, such as those of a collective nature.

The contribution to states which are formed by second, or higher, order processes (e.g., the reaction proceeds through an intermediate state to the final state of the target) must be calculated through higher order terms in DWBA. However, in the CC-calculation, these contributions are automatically included, provided that the

intermediate states are included among the channels considered.

Coupled-Channel Calculation

The CC-calculations for the present work were done using the Oregon State University CDC 3300 computer and the programs developed by Schmittroth and Stomp (53, 46 see especially p. 114-140) employing the microscopic model of Madsen (29).

The total wave function is expanded in terms of a basis set of functions. Each function of the set is a product of a nuclear wave function and a projectile wave function. Writing the wave function for the total system, projectile plus target, in the notation of Schmittroth (46, p. 7-8),

$$\psi = \frac{1}{r} \sum_{\substack{Jn \\ j_n \ell_n}} R_{Jn\ell_n j_n}(r)[\mathcal{Y}_{\ell_n j_n} \Phi_{I_n}]_{JM} \tag{3}$$

where

$$[\mathcal{Y}_{\ell_n J_n} \Phi_{I_n}]_{JM} = \sum_{\substack{m_j \\ M_n}} C(j_n I_n J; m_j M_n M) \mathcal{Y}_{\ell_n j_n m_j} \Phi_{I_n M_n} \tag{4}$$

and

$$\mathcal{Y}_{\ell_n j_n m_j} = [i^{\ell_n} Y_{\ell_n} \Sigma_s]_{j_n m_j} \tag{5}$$

is the angular momentum part of the projectile wave function of total angular momentum j_n, z-projection m_j and orbital angular momentum ℓ_n. Φ_{I_n} is the nuclear bound state wave function for channel n with nuclear spin I_n and z-projection M_n. Σ_s represents the spin and isospin parts of the projectile wave functions with spin S. $R_{J n \ell_n j_n}(r)$ are the radial wave functions for the projectile whose center of mass is at r. The $C(j_1\ j_2\ J;\ m_1\ m_2\ M)$ are Clebsch-Gordan coefficients representing the vector sum of j_1 and j_2 equal to J and $M = m_1+m_2$. Y_{ℓ_n} is a spherical harmonic function (with the angular arguments and m_{ℓ_n} quantum number supressed). J is the total angular momentum for the system and M its z-projection.

Inserting this form of ψ_n into the Schroedinger equation, $H\psi = E\psi$, multiplying from the left by $[\mathcal{Y}_{\ell_{n'} J_{n'}} \Phi_{I_{n'}}]_{JM}$, and integrating over all coordinates except r,

$$\left[-\frac{\hbar^2}{2m}\frac{d^2}{dr^2} + \frac{\ell_n(\ell_n+1)}{r^2} + V_{nn}(r) - E + E_n\right] R_{J n \ell_n j_n}$$

$$= -\sum_{\substack{n' \neq n \\ \ell_{n'} j_{n'}}} V_{nn'}(r) R_{J n' \ell_{n'} j_{n'}}(r) \tag{6}$$

where

$$V_{n'n}(r) = \left\langle [\mathcal{Y}_{\ell_{n'} j_{n'}} \Phi_{I_{n'}}]_{JM} \middle| V \middle| [\mathcal{Y}_{\ell_n j_n} \Phi_{I_n}]_{JM} \right\rangle . \tag{7}$$

E_n is the excitation energy or Q value to the nth channel, while E is the incident energy of the projectile.

In the calculation, the diagonal terms of the potential, V_{nn}, are replaced by an optical potential, then Equation (6) reduces to the optical model for $n = n'$. The general form of the optical potential used is

$$V(r) = -V_r f_r(r) - iW_v f_v(r) - i4a_s W_s\left(-\frac{df_s}{dr}\right) - V_{so}(\vec{\ell}\cdot\vec{\sigma})\left(\frac{\hbar}{m_\pi c}\right)^2\left(-\frac{1}{r}\frac{df_s}{dr}\right) \tag{8}$$

where

$$f_x(r) = \left[1 + e^{\left(\frac{r-R_x}{a_x}\right)}\right]^{-1} \tag{9}$$

for $x = r, v, s$, while m_π is the pion rest mass. The values for the optical parameters used are given in Table 1. They are based on the values of Perey (35) and were modified by a trial and error method to give a best fit (determined by inspection) to the elastic scattering data of the present experiment (Figure 10).

The microscopic potential used in forming the off diagonal terms, $V_{nn'}(r)$, is

$$V(r) = \left[(V_{00}+V_{10}\vec{\sigma}_1\cdot\vec{\sigma}_2) + (V_{01}+V_{11}\vec{\sigma}_1\cdot\vec{\sigma}_2)\vec{\tau}_1\cdot\vec{\tau}_2\right]v_C(r) + V_T S_{12}\vec{\tau}_1\cdot\vec{\tau}_2 V_{12}(r)\,. \tag{10}$$

Table 1. Optical model parameters.

Reaction	E_p (lab)	Q	V_r	W_s	V_{so}	R_x (Fermis)
$^{14}N(p,p)^{14}N$, g.s.	17.2	0.0	-45.0	-4.5	-5.0	3.01
$^{14}N(p,n)^{14}O$, g.s.	17.2	-6.0	-48.3	-4.5	-5.0	3.01
$^{14}N(p,p')^{14}N$, 2.3-MeV state	17.2	-2.319	-46.3	-4.5	-5.0	3.01
$^{14}N(p,p')^{14}N$, 3.9-MeV state	17.2	-3.952	-47.2	-4.5	-5.0	3.01
$^{15}N(p,p)^{15}N$, g.s.	17.3	0.0	-46.7	-5.2	-5.5	3.08
$^{15}N(p,n)^{15}O$, g.s.	17.3	-3.542	-48.6	-5.2	-5.5	3.08
$^{15}N(p,p')^{15}N$, 6.3-MeV state	17.3	-6.323	-50.2	-5.2	-5.5	3.08
$^{15}N(p,n')^{15}O$, 6.2-MeV state	17.3	-9.710	-51.9	-5.2	-5.5	3.08

All strengths and energies are in MeV, $W_v = 0$, and $a_r = 0.65$ fm, $a_I = 0.47$ fm, and $a_{so} = 0.65$ fm for all reactions.

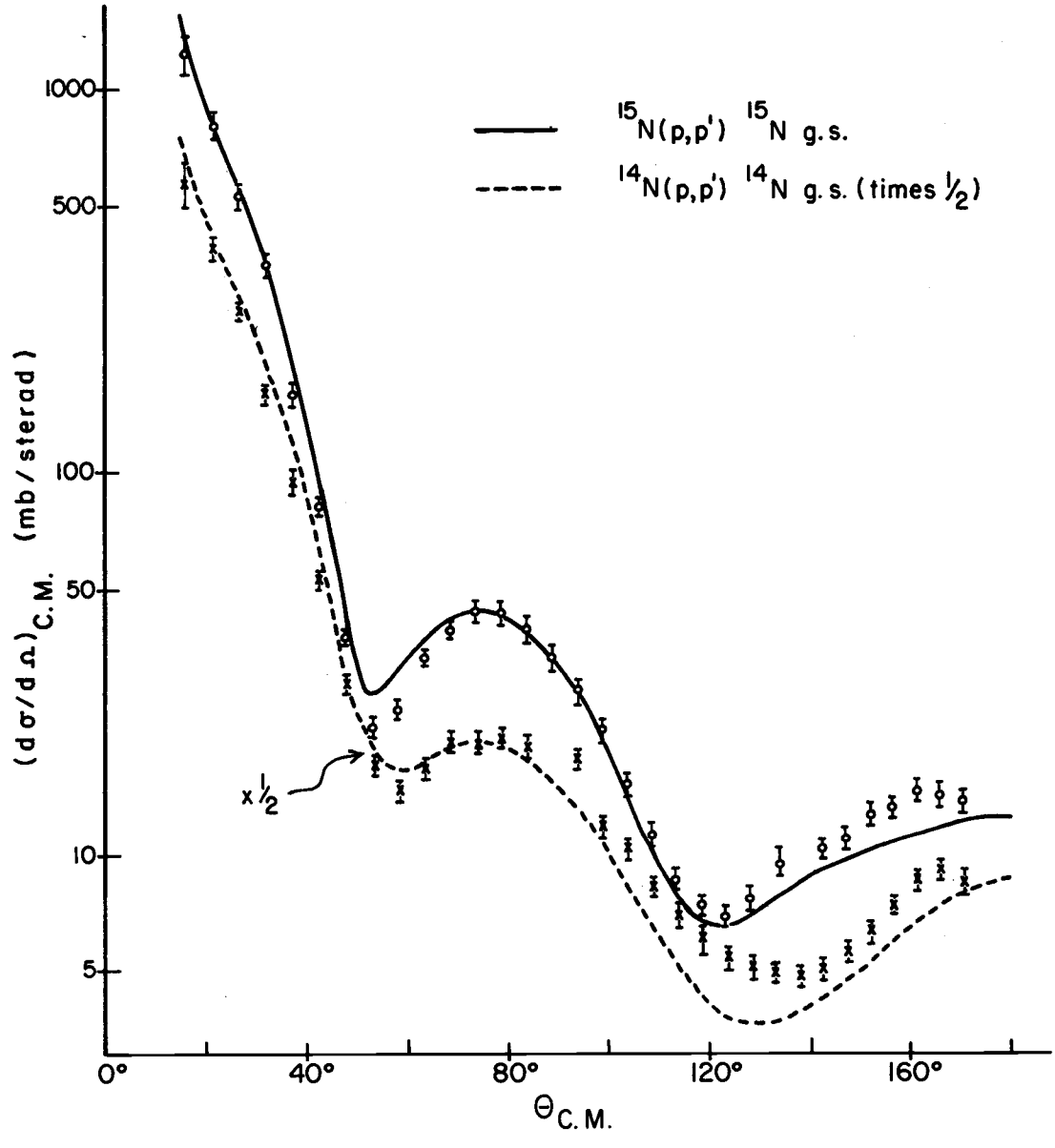

Figure 10. Ground state angular distributions and optical model fit for ^{15}N and ^{14}N. A scale factor of 1/2 was used for both the ^{14}N data and fit to avoid overlap with the ^{15}N data.

The four central strengths are of the form V_{ST}, where S and T are the changes of the z-components of the spin and isospin respectively, of the projectile. The values used for the strengths are those of Petrovitch et al. (36), and are given in Table 2. These values were derived from the Kallio-Koltveit spin dependent two-body potential which itself is derived from a free nucleon-nucleon potential (25).

The radial parts of Equation (10) are

$$V_c(r) = \frac{e^{-ar}}{ar} , \tag{11}$$

and

$$V_{12}(r) = E(a_T r) - (b/a)^3 E(b_T r), \tag{12}$$

where

$$E(xr) = (1/(xr)^2 + 1/(xr) + 1/3) \frac{e^{-xr}}{xr} , \tag{13}$$

and finally

$$S_{12} = 3\left[\frac{3(\vec{\sigma}_1 \cdot \vec{r})(\vec{\sigma}_2 \cdot \vec{r})}{r^2} - \vec{\sigma}_1 \cdot \vec{\sigma}_2\right] \tag{14}$$

Table 2. Microscopic potential strengths (MeV).

V_{00}	V_{01}	V_{10}	V_{11}	V_T
-36.2	17.8	6.23	12.1	4.0

Central inverse range, a = 1 fm.

Tensor inverse ranges, a_T = 0.714 fm and b_T = 4.0 fm.

The bound state wave functions, Φ_{I_n}, are found as solutions to the Schroedinger equation

$$[\frac{\hbar^2}{2m}(-\frac{d^2}{dr^2}+\frac{\ell(\ell+1)}{r^2})+V(r)-E]u(r)=0 \qquad (15)$$

where

$$V=-V_o[F(r)-C_{LS}(\frac{\vec{\ell}\cdot\vec{\sigma}}{2})\lambda_\pi^2\frac{1}{r}\frac{dF(r)}{dr}] \qquad (16)$$

and

$$F(r)=[1+e^{(\frac{r-R}{a})}]^{-1}. \qquad (17)$$

λ_π is the pion compton wave-length, $R = 1.25 \times A^{1/3}$ (A = the mass number), $a = 0.65$ fm, $C_{LS} = 0.278$, and E is the binding energy. The potential used (Equation 16) is a simplified form of Equation (8), which takes advantage of the fact that the results of the CC calculation are relatively insensitive to changes in the bound state wave functions.

The computer routine first integrates Equation (15) inward from $r = 10$ fm until the function turns over. The function is then integrated outward from the origin and matched to the results of the inward integration. V_0 is then adjusted until the match provides a smooth curve. The binding energies used and the resulting well depths, V_0, are given in Table 3. The binding energies are those obtained by Schmittroth (46, p. 121). The 9.0 MeV binding of the

$p_{1/2}$ state is an average of the neutron separation energies in ^{14}C and ^{14}N; the 6.0 MeV difference between the $p_{1/2}$ and $p_{3/2}$ states is approximately the splitting seen in ^{15}N and ^{15}O (1). The binding energies given for the $1d_{5/2}$ and the $2s_{1/2}$ states are from the neutron separation energies of O^{17} and the first excited $1/2^+$ state in ^{17}O, respectively (1, 46, p. 116-117). The binding energies for mass 14 are taken to be slightly greater than those for mass 15 in order to get binding for a $d_{3/2}$ particle.

Table 3. Single-particle bound state parameters.

State	V_0 (MeV)	Binding Energy (MeV)
Mass 15		
$p_{1/2}$	48.5	9.0
$p_{3/2}$	51.4	15.0
Mass 14		
$p_{1/2}$	53.4	10.5
$p_{3/2}$	55.5	16.65
$2s_{1/2}$	59.6	3.25
$d_{3/2}$	69.2	0.5
$d_{5/2}$	58.5	4.15

Using a simple shell model for the mass 15 system and the wave functions of Visscher and Ferrell (55) for the mass 14 system, spectroscopic factors (which describe the probability of single particle transitions within the target nucleus) were calculated using the

formulas of Madsen (29). These spectroscopic factors contain information about the nucleus and represent it in a form (single particle transitions) necessary for calculations with the microscopic potentials, which are two body operators.

To obtain a cross section, the system of Equations (6) is solved for $R_{Jn\ell_n j_n}(r)$. At large distances from the target, the wave function is required to become a superposition of outgoing and incoming spherical waves. The scattering matrix is then formed, and from this the differential cross sections may be calculated. A detailed description is given by Stomp (53).

Tensor Force

The necessity of including a tensor component as part of the nuclear force has been considered for some time (see, e.g., 47, 55, 60). More recently, Rose et al. (40), conclude that without a tensor force, even if one does use configuration mixing (including contributions from configurations other than the most simple shell-model configuration which have the same quantum numbers), the matrix elements for beta and gamma decay from low-lying states in the mass fourteen system cannot simultaneously be fit by the theory. However, when they include a tensor force, they obtain a good fit between experiment and theory. The addition of configuration mixing to the tensor force results in some additional improvement.

The above results agree with Schmittroth (46, p. 109) who found it necessary to include a tensor force in order to fit $^{14}C(p,n)^{14}N$ data (E_p = 13.7 MeV) and $^{14}N(p,p')$ data (2.31-MeV state, E_p = 24.5 MeV) by a DWBA calculation employing a microscopic model. He also found some improvement by including a tensor force in a fit to $^{15}N(p,n)^{15}O$ data (6.2-MeV state, E_p = 18.8 MeV).

Crawley et al. (12) find that the inclusion of a tensor force of the form used in the present work greatly improves a fit to $^{14}N(p,p')^{14}N$ data (2.31-MeV state, E_p = 24.8 MeV). The strength used in the present work was 4.0 MeV using the same normalization as Crawley et al., who cite a value of 3.9 MeV. The form of the tensor potential used is given above in Equations (10 and 12-14).

Weak-Coupling Model

Consider a nucleus which may be described as a single particle (or hole) outside a core. Suppose further that the core may be described as a collective excitation in a nearly spherical even-even nucleus. In the approximation of extremely weak coupling between the particle and the core, the states of an odd-A nucleus may be represented as simply products of the eigenfunctions of the odd nucleon $|jm>$ with the eigenfunctions of the collective core $|\ell m'>$. In this case, one can show (9) that the cross section to a definite state I' in the odd-A nucleus with an angular momentum transfer ℓ is

related by a simple statistical factor to the cross section for collective excitation in the neighboring even-even nucleus

$$\frac{d\sigma}{d\Omega}(\ell; I \rightarrow I') = \frac{(2I'+1)}{(2\ell+1)(2I+1)} \frac{d\sigma}{d\Omega}(0 \rightarrow \ell). \tag{18}$$

Further, the statistical factor summed over $|I-\ell| \leq I' \leq (I+\ell)$ equals unity. Thus the sum of all pertinent cross sections in the odd-A nucleus should equal the cross section for the pertinent collective excitation in the neighboring even-even nucleus.

Bussiere et al. (10), describe the 5.27-MeV $(5/2^+)$ and the 7.56-MeV $(7/2^+)$ states in ^{15}N as a $p_{1/2}$ proton hole coupled to the 6.134-MeV (3^-) state of ^{16}O. They compared the cross sections from inelastic alpha scattering to the above states and found them to be similar in shape and approximately the magnitude predicted by weak coupling (Equation (18)). In a second paper by the same authors (20), they suggest that the 5.304-MeV $(1/2^+)$ and the 7.31-MeV $(3/2^+)$ levels of ^{15}N may be related to the 7.115-MeV (1^-) level of ^{16}O. Their experiment did not resolve the 5.304-MeV level, but they find the angular distribution of the 7.31-MeV level to be similar to that of the 7.115-MeV level of ^{16}O. They also conclude that the 6.32-MeV $(3/2^-)$ level of ^{15}N appears to be related to the $p_{3/2}$ to $p_{1/2}$ single-particle transition rather than to the 6.916-MeV (2^+) level of ^{16}O (from which it would be formed in the extreme weak-coupling model).

A weak-coupling model for the 6.32-MeV ($3/2^-$) state of ^{15}N has been considered in a series of articles (2, 17, 18, 21, 28, 37, 41-43, 45, 48, 56, 58). A summary of most of the development is given by Gill et al. (18). The essence is that the E2/M1 mixing ratios for the 6 MeV to ground state transitions in ^{15}O and ^{15}N showed (28) that the electric quadrupole matrix element was larger in ^{15}O than ^{15}N. This result cannot be explained in terms of the independent particle model. Stripping and pick-up reactions (23, 31, 58) have indicated that the $p_{3/2}$ hole states are predominantly located at 6.32 MeV and 6.18 MeV in ^{15}N and ^{15}O respectively.

To explain the mixing ratios, Lopes et al. (28), considered a model in which a collective admixture is present in the wave function of the 6-MeV states. Their model is more complex than the extreme weak-coupling model in that the parent 2^+ state of ^{16}O coupling to a $p_{1/2}$ hole state contributed as part of the wave function of two separate $3/2^-$ states in ^{15}N, rather than comprising the complete wave function for a single such $3/2^-$ state. A calculation using this weak coupling approximation (42) showed that mixing some amplitude (15% intensity is the maximum consistent with the pick-up data (42)) of a state formed by coupling a $p_{1/2}$ hole to the first excited 2^+ state of the ^{16}O core with the pure $p_{3/2}$ hole state resulted in fair agreement with the experimental value of the ^{15}N E2/M1 mixing ratio, but it was not possible to reach an agreement in the ^{15}O case.

Shukla and Brown (48) present a calculation using the random phase approximation in which they mixed into the 6-MeV single-hole states large amplitudes of two-particle-three-hole excitations. They then find good agreement for the mixing ratio for ^{15}O, but the ^{15}N value is considerably too large (by a factor of two).

Shukla and Brown find that the mixing of the single-hole state with two-particle-three-hole configurations in amplitudes consistent with experimental data implies that there should be a large amplitude of the $p^{-1}_{3/2}$ state concentrated at another state which they place at about 9 MeV. This state is not detected in a pick-up reaction (58) on ^{16}O because in the upper (9 MeV) state the single-hole and collective contributions to the pick-up amplitude interfere destructively (48), while for the lower state they add constructively.

The weak-coupling model employed by Rose and Lopes (17, 18, 21, 28, 41-43) also requires a largely collective $3/2^-$ state at about 9 MeV. One member of the doublet at 9.16 MeV in ^{15}N (Figure 7) has been identified as $3/2^-$ (its apparent analog $3/2^-$ state in ^{15}O is at 8.98 MeV) (49) and as the state required by the weak coupling model of Rose and Lopes (see, e.g., 18, 56).

The positive parity states of ^{15}O and ^{15}N are generally interpreted as shell model states (19, 38, 57), or as weak-coupling model states formed from parent states in ^{16}O. However, a different weak-coupling model for the low-lying, positive-parity states has been

considered by Lane (27) and more recently by Phillips and Jacobs (37). They find the best fit to $^{14}N(d, p)^{15}N$ data by using a weak-coupling model in which an $s_{1/2}$ or $d_{5/2}$ particle is coupled to the ground or first excited state of ^{14}N. They include an isospin term

$$\vec{T} \cdot \vec{t} = \frac{1}{2}[T_f(T_f+1) - T(T+1) - t(t+1)] \qquad (19)$$

where T is the isospin of the ^{14}N core state, t is the isospin of the odd particle outside the core, and T_f is the isospin of the resultant state in ^{15}N. With this model they are able to reproduce most of the known features of the levels, including the position of the 5.3-MeV doublet. In this model, the $1/2^+$ member of the doublet is formed by coupling an $s_{1/2}$ proton to the first excited state of ^{14}N, while the $5/2^+$ doublet member is formed by coupling a $d_{5/2}$ proton to the same ^{14}N core state.

IV. RESULTS AND DISCUSSION

Figure 7 shows the energy level diagrams for the nitrogen isotopes of interest, and Figures 8 and 9 show typical spectra for ^{15}N and ^{14}N respectively. The excited states were identified by measuring the energy of the scattered proton. Figure 10 shows the ground state angular distributions for both nitrogen isotopes. The theoretical curves are optical model fits using the parameters of Table 1.

Excited States of ^{15}N

Six states and doublets were resolved well enough to yield experimental cross sections over a large angular range. Experimental angular distributions are shown for the doublet at 5.3 MeV (Figure 16), the 6.32-MeV state (Figure 11), the doublet at 7.2 MeV (Figure 17), the state at 7.56 MeV (Figure 16) and the states at 8.31 and 8.57 MeV (Figure 18). The error bars shown include uncertainties due to statistics, background subtraction, and a possible 6% error in absolute normalization.

The most extensive theoretical analysis was done for the 6.32-MeV $3/2^-$ state. Using the coupled-channel code described previously, calculations were done in which two channels were coupled (2CC), (the ground and 6.32-MeV states), and in which four channels were coupled (4CC). Inspection of the gamma decay scheme (49) shows that

none of the other low-lying ^{15}N states couple with the 6.32-MeV state. In the 4CC calculation the ground and 6.32-MeV states of ^{15}N were coupled together with their analog states, the ground and 6.2-MeV states of ^{15}O. The result of each calculation was multiplied by a normalization factor in order to give the best fit to the data as determined by inspection. The normalization factors may represent core polarizations or other inadequacies of the wave functions or may reflect uncertainties in the magnitude of the microscopic potentials. The normalizations are given in Table 4. Since the microscopic potential strengths are themselves normalized for the inverse ranges given in Table 2, normalization factors are not given in Table 4 for calculations in which the inverse ranges were changed. Since the strengths were not renormalized to correspond to the new inverse ranges in these calculations, a final normalization to fit the data lacks physical significance. The same comment applies to the calculations in which a form factor was artificially introduced (without compensating the strengths).

Consider the 6.32-MeV state of ^{15}N. The 2CC calculation (Figure 11) is nearly the correct magnitude (normalization factor 1.17); however the shape of the theoretical curve leaves much to be desired. The theoretical curve does not fit the peak at small angles and is out of phase with the data beyond 100°. The 2CC-no tensor calculation is clearly worse in shape, both at small angles and at 110°.

The normalization factor, 1.75, is also larger. The 4CC calculation is again nearly correct in magnitude (normalization 0.84), and is a slight improvement at 110°, but it is slightly worse at small angles than the 2CC calculation.

Table 4. Normalization factors.

Reaction/Normalization Point	Calculation	Normalization
$^{15}N(p,p')^{15}N$, 6.3-MeV state	2CC	1.17
(Normalized to .7 @ 90°)	2CC-no tensor	1.75
	4CC	0.84
	4CC-enhanced	0.46
$^{15}N(p,n)^{15}O$ (data at 18.8 MeV)		
Ground State		
(Normalized to 2 @ 50°)	4CC	0.43
	4CC-enhanced	0.22
6.17-MeV State		
(Normalized to 2 @ 0°)	4CC	0.72
	4CC-enhanced	0.68
$^{14}N(p,p')^{14}N$		
2.3-MeV State		
(Normalized to 1.07 @ 70°)	4CC	1.0
	4CC-no tensor	3.1
3.9-MeV State		
(Normalized to .8 @ 90°)	4CC	4.2
	4CC-no tensor	4.8

To take into account any collective enhancement that would result if the 6.32-MeV state were not a simple $p_{3/2}$ proton hole state but also contained a collective component, effective charges were

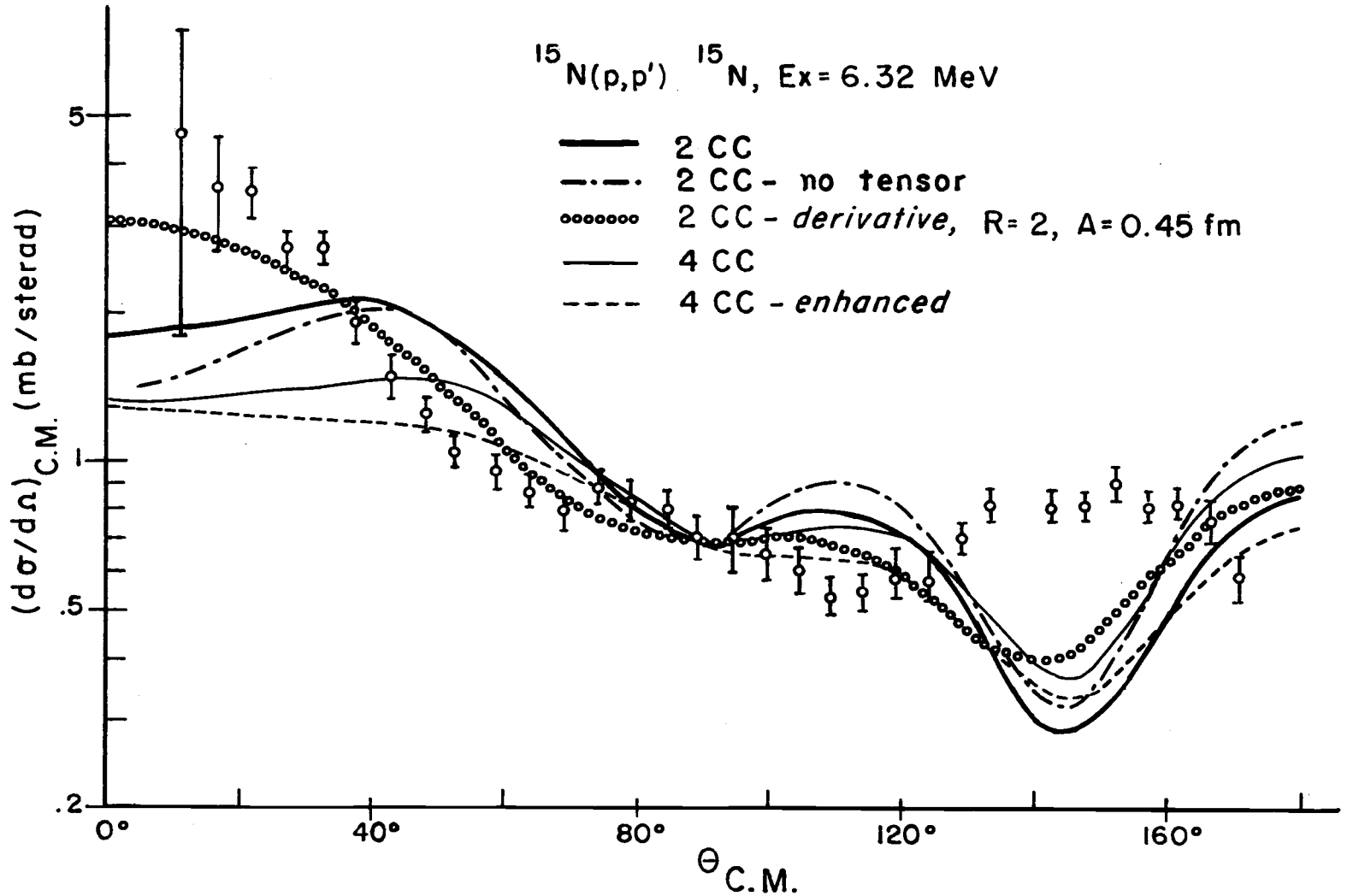

Figure 11. Angular distribution for the 6.32-MeV state of ^{15}N and comparison with theory. The abbreviations used are defined in the text.

calculated. Assigning an effective charge to a nucleon is a way of taking into account collective motion of the nucleons of the core in which they all move together. This collective motion is not present in the simplest shell model. Such a simple model could not correctly predict an elctromagnetic transition rate from a collective state, for example. The ratio of a measured transition probability to that predicted by the simple shell model is a measure of the collectiveness or non-single-particle nature of a state. The square root of this ratio, corresponding to a transition amplitude enhancement, is a collective enhancement factor which can be used to improve the simple shell model. Since electromagnetic transition and inelastic scattering amplitudes are closely related (5), the collective enhancement factor derived from electromagnetic transition rates can be used to predict an enhancement in inelastic scattering.

Using the electric dipole transition probability of 7.65 ± 2.55 e^2fm^4 as extracted from the level width given by Beer *et al.* (8), and the single particle value of 4.38 e^2fm^4, a proton enhancement factor of 1.32 ± 0.26 is extracted according to the definition of Atkinson and Madsen (5).

$$e_p = \sqrt{\frac{7.65 \pm 2.55}{4.38}} \simeq 1.32 \pm 0.26 \qquad (20)$$

(This value compares favorably with the median value of 1.35

calculated by Shukla and Brown (48).) The corresponding neutron enhancement (5) was taken to be 0.4 ± 0.2.

$$e_n = e_p - 1 \simeq 0.4 \pm 0.2 \tag{21}$$

Using the maximum enhancement implied by these values, the microscopic potential strengths become (5):

$$\begin{aligned} V_{00} &\rightarrow V_{00}(e_p+e_n) \simeq V_{00} \times 2 = -72.4 \text{ MeV} \\ V_{01} &\rightarrow V_{01}(e_p-e_n) \simeq V_{01} \times 1.2 = 21.4 \text{ MeV} \end{aligned} \tag{22}$$

With V_{10}, V_{11}, and V_T remaining the same since only the zero isospin transfer terms are enhanced (5).

A 4CC calculation was done using the maximum enhancement permissible according to the above calculations. The results (Figure 11) fit the data better than the simple 4CC calculation at 110°. The curve also shows a slight peak at small angles but clearly misses the data. Including the collective enhancement seems to help the shape, but the fit to the data is still not very good, and the normalization is worse.

Figure 12 shows the results of using different inverse ranges in the microscopic potential. Normally an inverse range of 1.0 fm is used. A long range force (inverse range of 0.5 fm) gives a reasonable fit from 40° to 120°, but misses the small angle peak. A short range

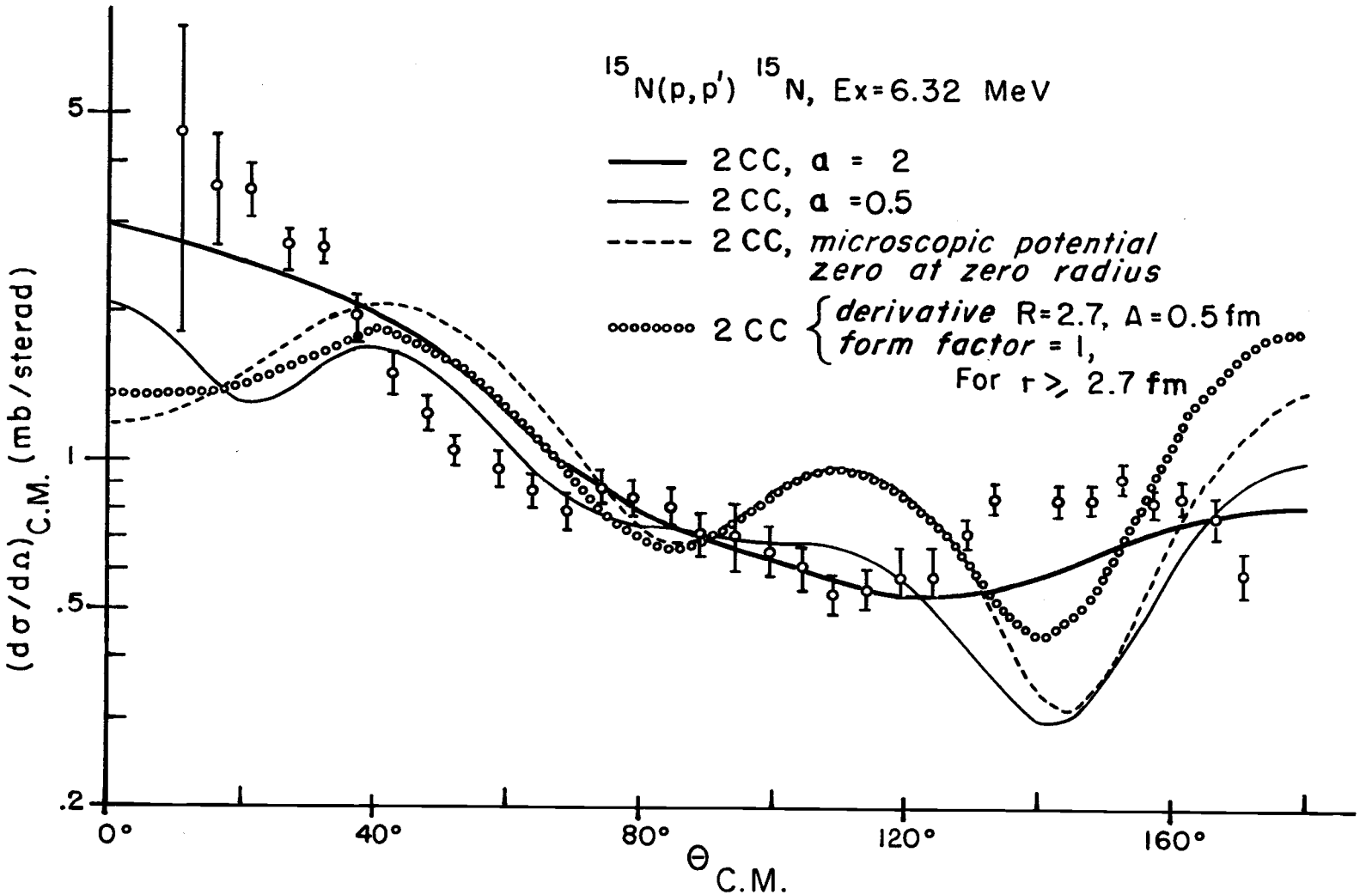

Figure 12. Angular distribution for the 6.32-MeV state of ^{15}N and comparison with the theory. "a" is the microscopic potential inverse range. Other abbreviations are defined in the text.

force (inverse range of 2.0fm) gives a reasonable fit from 0° to 125°, but the physical significance of such a short range for the nuclear force is highly questionable.

Since the potential used does not specifically contain a hard core, an attempt was made to account for the effects of a hard core by simulating the G matrix (36). The G matrix does account for the hard core. The radial form factor for the microscopic potential was taken to be formed by the sum of three Yukawa wells so normalized that the potential goes to zero at zero radius. The results (Figure 12) were simply a greater amplitude in the oscillations of the theoretical curve.

The coupled-channels calculation used does not employ antisymmetrized wave functions and therefore neglects the Pauli exclusion principle (PEP). To estimate the effect of incorporating the PEP, it was decided to introduce a radial density form factor. The aim was simply to take into account the decreasing probability of the incoming proton to penetrate deeply into the target nucleus (see Negele (33)). The form factor used was

$$F = \begin{cases} G(r) & r \leq R \\ 1 & r > R \end{cases} \tag{23}$$

where

$$G(r) = \frac{4}{e^{(\frac{r-R}{A})} + e^{-(\frac{r-R}{A})} + 2} \tag{24}$$

is the derivative of a Woods-Saxon well of radius R and diffuseness A. The normalization is such that $G(r) = 1$ at $r = R$. In effect, this form factor simply multiplied the nuclear wave function in the calculation.

The result, using a 2CC calculation, (Figure 12) was quite similar to that of forcing the potential to zero at zero radius. The calculation shown has $R = 2.7$ fm, $A = 0.5$ fm compared with $R = 3.08$ fm and $A = 0.65$ fm for the target nucleus well parameters. Both larger and smaller values of R and A were tried in the form factor (Equation (23)) with results similar to those shown (Figure 12).

A simpler form factor was also tried:

$$F = G(r) \quad \text{for all} \quad r. \tag{25}$$

The results, using a 2CC calculation, are shown in Figure 13 for various values of R and A. It was found that fairly good fits were obtained for values of R between about 2.0 and 2.7 fm. Inspection shows that there is a peak in the target nucleus wave function used which lies between these two values. The peak itself is at 2.4 fm. The best fit to the data is for $R = 2.0$ fm and $A = 0.45$ fm (shown in Figure 13 and again for comparison in Figure 11).

In trying to understand any physical meaning attached to the derivative form factor (Equation (25)), note that the best result using

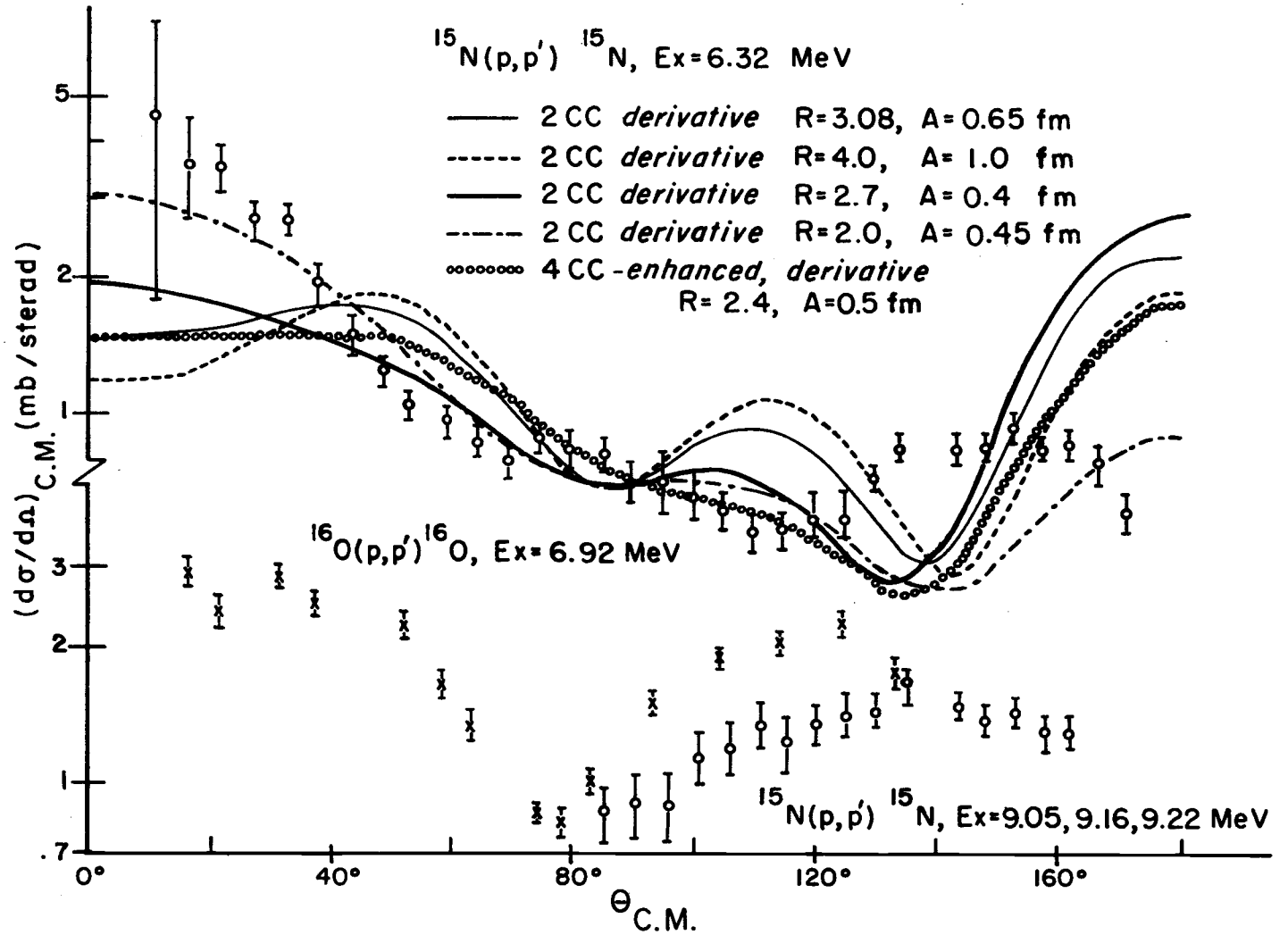

Figure 13. Angular distributions for the first and second $3/2^-$ states of ^{15}N, and comparison with the theory. The oxygen data are from reference (13). Abbreviations used are defined in the text.

this form factor is similar in shape to that obtained using a short range force. In the limit of a zero range force, the direct and exchange contributions to the scattering amplitude are equal (3, 6). Therefore as the force range becomes shorter, the results of the direct calculation should become more like the results of the exchange calculation. It seems possible that the derivative form factor is simulating the effects of exchange. Calculations are being done to check this and the results will be reported in a future publication.

Finally, a 4CC calculation was done using the enhancement factors calculated above (Equation (22)) and including the derivative form factor. The results (Figure 13) are noticeably worse, especially at the forward peak, than the 2CC calculation with the derivative form factor. A strange result should not be surprising in view of the rather artificial form factor used. The more physical form factor would seem to be Equation (23). Other form factors were not used in the 4CC calculation because of the expense of doing a 4CC calculation.

Figure 14 shows the results of the 4CC calculation for the $^{15}N(p, n)^{15}O$, ground state reaction. The data are that of Anderson et al. (4), and are for $E_p = 18.8$ MeV compared with 17.3 MeV for the calculation. The experimental angular distribution at 13.6 MeV (4) is nearly flat at small angles, lacking the pronounced dip shown in Figure 14. One would suppose that at 17.3 MeV the dip would still be present, but less pronounced than at 18.8 MeV. There

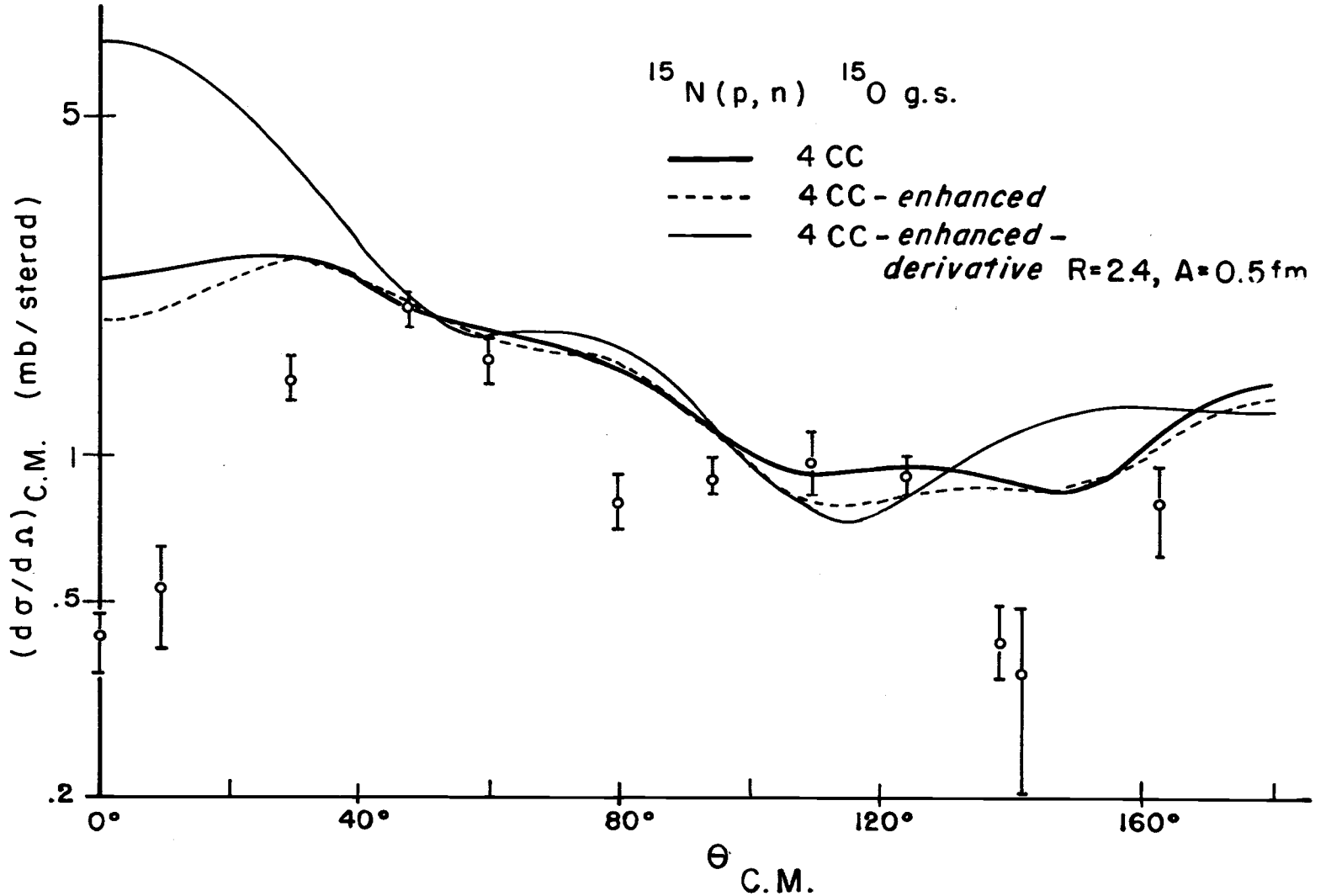

Figure 14. ^{15}N(p,n)^{15}O, ground state, reaction and comparison with the theory. The data are from Anderson et al. (4), and are for E_p = 18.8 MeV. Abbreviations used are defined in the text.

is little difference between the 4CC calculation and the 4CC calculation with enhancement. The enhanced calculation does have more of a dip at small angles and is therefore slightly better. The 4CC calculation including the derivative form factor is clearly worse.

Figure 15 shows the remaining state included in the mass 15 4CC calculation, the 6.17-MeV state of ^{15}O. Again the data is from Anderson et al. (4), and is for $E_p = 18.8$ MeV. The 4CC calculation with the derivative form factor is the worst. The data is not sufficiently accurate to allow a choice between the 4CC and 4CC-enhanced calculations, both fits being fairly good.

Weak-Coupling for ^{15}N

The weak-coupling model for the 6.32-MeV, $3/2^-$ state of ^{15}N relates this state to the 6.92-MeV, 2^+ state of ^{16}O. Figure 13 shows that these states are not related by the simple weak-coupling model predictions. Their shapes are not the same, nor is the magnitude of the ^{15}N state about 0.4 times (as predicted by Equation (18)) that of the ^{16}O state. The data for the ^{16}O state is that of Crawley and Garvey (13) for $E_p = 17.5$ MeV and has a possible error in absolute magnitude of ± 10%.

However, it is interesting to compare the ^{15}N angular distribution for the upper $3/2^-$ state at 9.16 MeV with the ^{16}O state (Figure 13). Unfortunately the upper $3/2^-$ state is a close doublet with

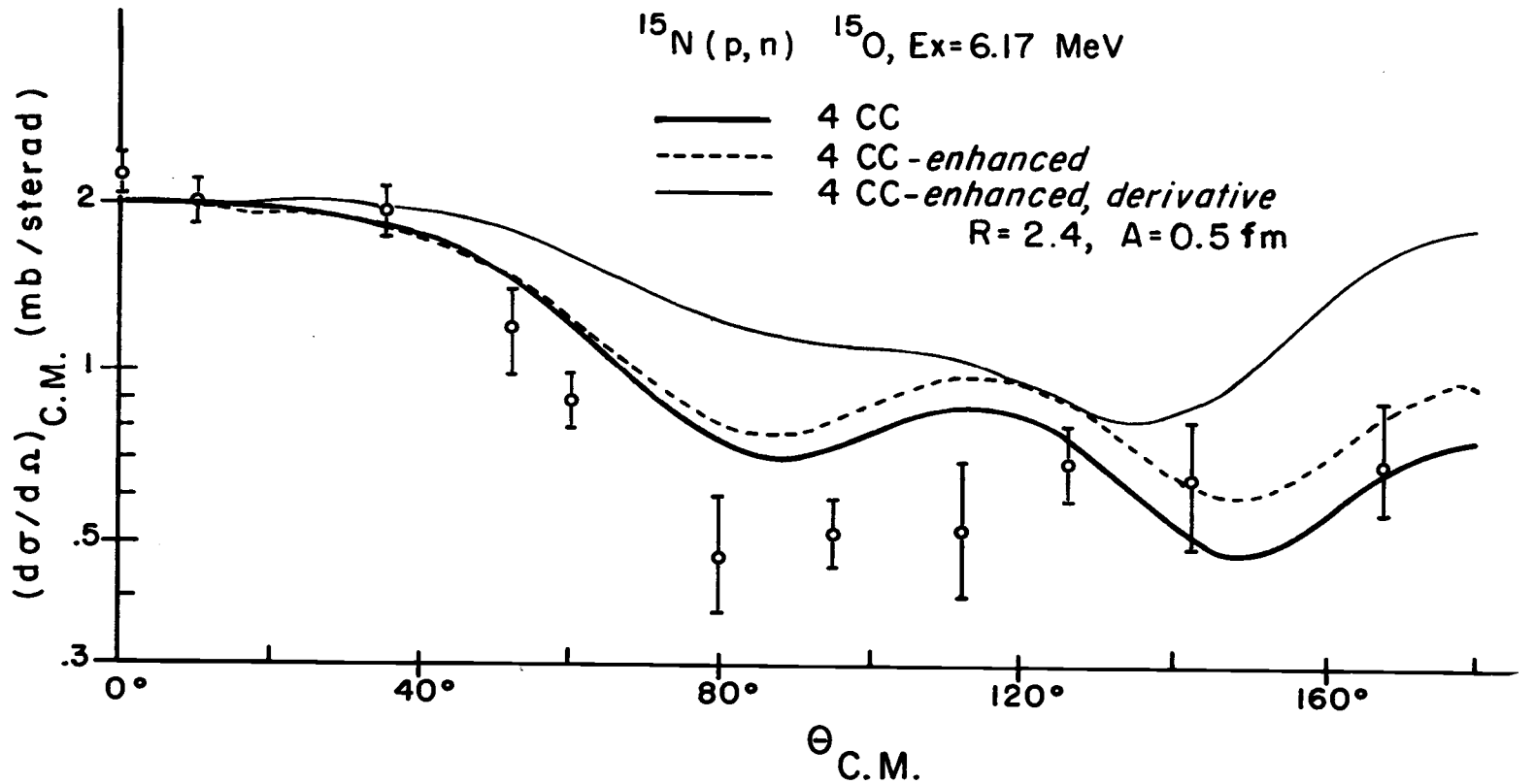

Figure 15. $^{15}N(p,n)^{15}O$, 6.17-MeV state, angular distribution and comparison with the theory. The data are from Anderson et al. (4), and are for E_p = 18.8 MeV. Abbreviations used are defined in the text.

additional states about 100 keV above and below it forming an unresolved quadruplet of states (Figure 7). However, the resolution was sufficient to determine if the states at 9.16 MeV were the major contributors to the quadruplet. For angles greater than 100°, the 9.16-MeV doublet was the major contributor. For this range of angles, the shape and magnitude (0.4 times the $^{16}O(p, p')^{16}O$, 6.92-MeV state, cross section) are consistent with that of the weak-coupling model. Since there are other contributions present, it is expected that the actual upper $3/2^-$ state cross section occurs on the lower portion of the error bars shown in Figure 13.

For angles less than 80°, the cross section to the ^{15}N quadruplet rises rapidly. At 60°--70° it is about 2mb/sterad. For angles less than 60°, it is approximately equal to the $^{16}O(p, p')^{16}O$, 6.92-MeV state cross section. Data points for the ^{15}N quadruplet are not shown for these angles because of uncertainty in the meaning of the data. It is clear from the shape and position of the peak in the energy spectrum that ^{15}N states other than the 9.16-MeV doublet contribute a significant (but unknown) amount to the quadruplet cross section for angles less than 80 degrees.[5]

---

[5] A careful analysis of the peak shape to give the probable contribution from the other quadruplet states may be possible for angles greater than 75°. Such an analysis was not done for two reasons. First, it would not significantly extend the range of useful data. Second, the contribution of several highly excited states of ^{14}N becomes important for angles less than 80°. Since the cross section to these

The conclusion that the upper $3/2^-$ state is mainly collective and is the weak-coupling model state rather than the 6.32-MeV state is in agreement with Shukla and Brown (48) and Rose and Lopes (42).

Figure 16 compares the 7.56-MeV, $7/2^+$ and the 5.27-MeV, $5/2^+$ states of ^{15}N with the 6.13-MeV, 3^- state of ^{16}O. The weak coupling model forms these two states of nitrogen by coupling a $p_{1/2}$ proton hole to the oxygen state. The 5.27-MeV nitrogen state is included as an unresolved doublet in Figure 16, but it is assumed to be the major doublet component. This assumption is based on the weak-coupling model, which forms the 5.30-MeV, $1/2^+$ doublet member from the 7.12-MeV 1^- state of ^{16}O. Specifically, for angles of 60° or less, the 6.13-MeV, 3^- ^{16}O state angular distribution has about twice the magnitude of the 7.12-MeV, 1^- ^{16}O state (13). Since the weak-coupling statistical factors (Equation (18)) for forming both ^{15}N doublet states are roughly the same, it follows that the $1/2^+$ doublet member should contribute about 1/3, and the $5/2^+$ member about 2/3, of the

---

^{14}N states was not measured in the present experiment and could only be estimated, it was felt that the combined probable error in level location and background subtraction did not justify a more detailed analysis. However, since the ^{15}N quadruplet cross section is at least equal to that for $^{16}O(p, p')^{16}O$ (6.92-MeV state) reaction for angles less than 80°, the experimental data are not inconsistent with the weak-coupling model for the 9.16-MeV ^{15}N state. An inconsistency would occur if the ^{15}N data were significantly less than 0.4 times the ^{16}O cross section.

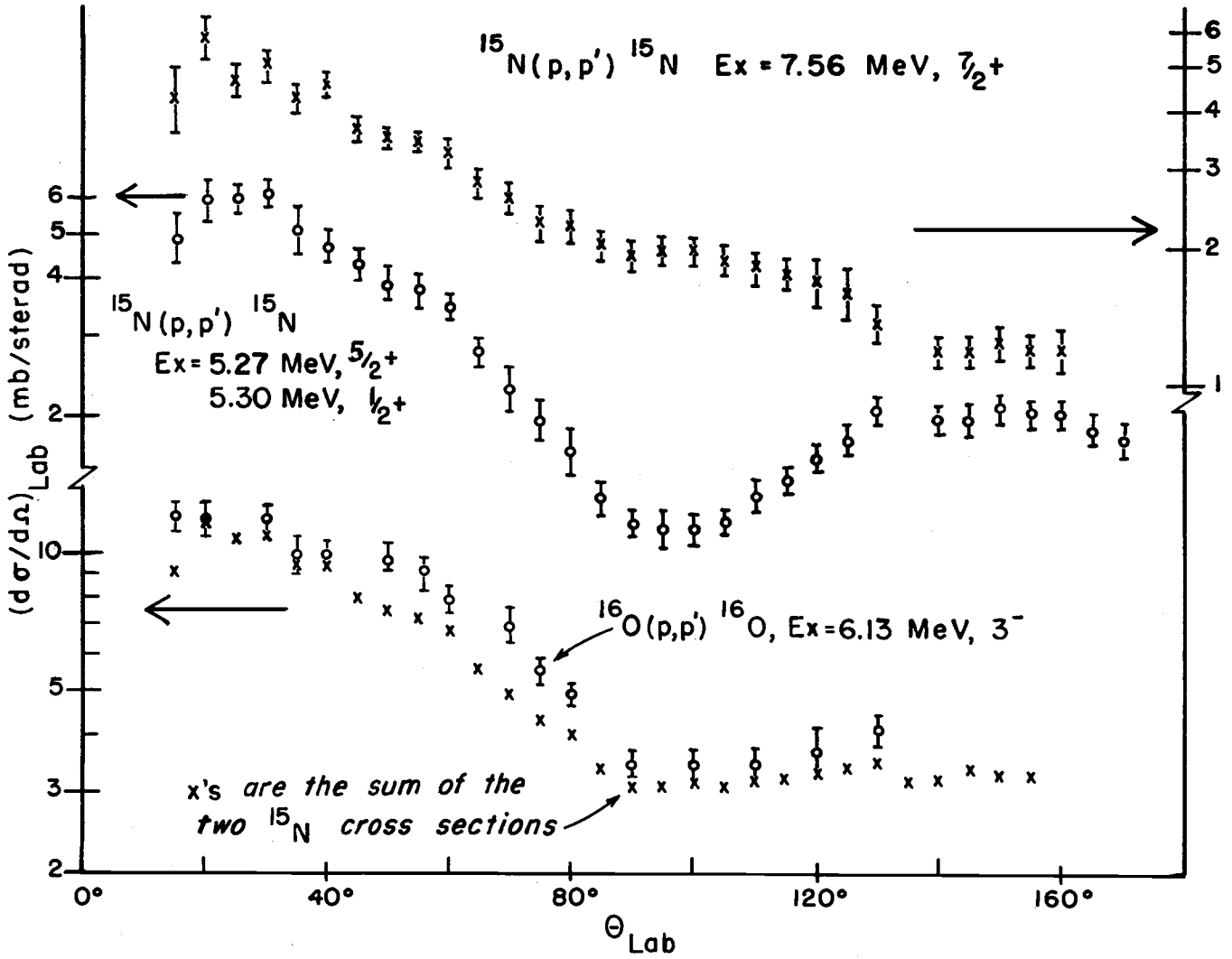

Figure 16. Angular distributions for the 7.56-MeV state and the 5-MeV doublet of ^{15}N compared with the 6.13-MeV state of ^{16}O (reference 13) for E_p = 17.5 MeV.

measured doublet cross section.

In Figure 16, the sum of the cross sections of the 7.56-MeV, $7/2^+$ and the 5.3-MeV doublet of ^{15}N are compared with the 6.13-MeV, 3^- state of ^{16}O. The oxygen data are that of Crawley and Garvey (13). As shown in the figure, both the shape and magnitude of the combined cross sections are in excellent agreement with the weak coupling model, consistent with the results of Bussiere et al. (10).

Figure 17 compares the 7.30-MeV, $3/2^+$ and 5.30-MeV, $1/2^+$ states of ^{15}N with the 7.12-MeV, 1^- state of ^{16}O (data from (13)). Comparison with the weak coupling model is difficult, because the ^{15}N states are members of unresolved doublets. Bussiere et al. (10) found the $5/2^+$ state at 5.27 MeV to be the state of the weak-coupling model, not the $5/2^+$ state at 7.15 MeV; we may assume that the 7.15 MeV state is not collectively enhanced, and thus its contribution is small.

Inspection of Figure 17 shows that 1/3 times the 5.3-MeV doublet cross section added to the 7-MeV doublet cross section results in a good fit to the ^{16}O state out to about 90°. Although the fit is worse beyond 90°, the weak coupling model for these states seems to be verified. Obviously an experiment which resolves the doublets, or which can be demonstrated to selectively excite only one member of the doublet (see, e.g., (10)), is necessary for a more conclusive interpretation.

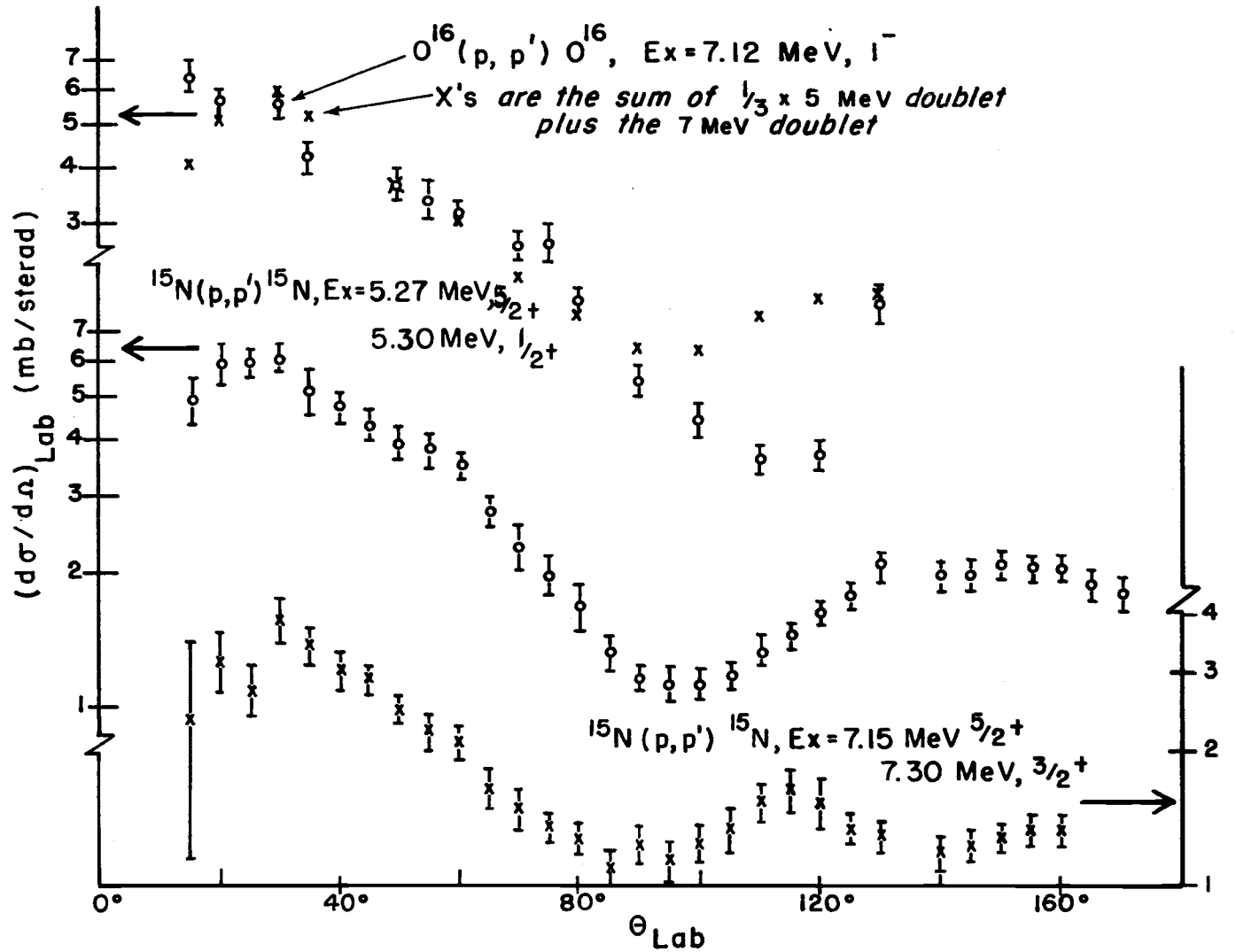

Figure 17. Angular distributions for the 5.3- and 7.2-MeV doublets of ^{15}N compared with the 7.12-MeV state of ^{16}O (reference 13) for E_p = 17.5 MeV.

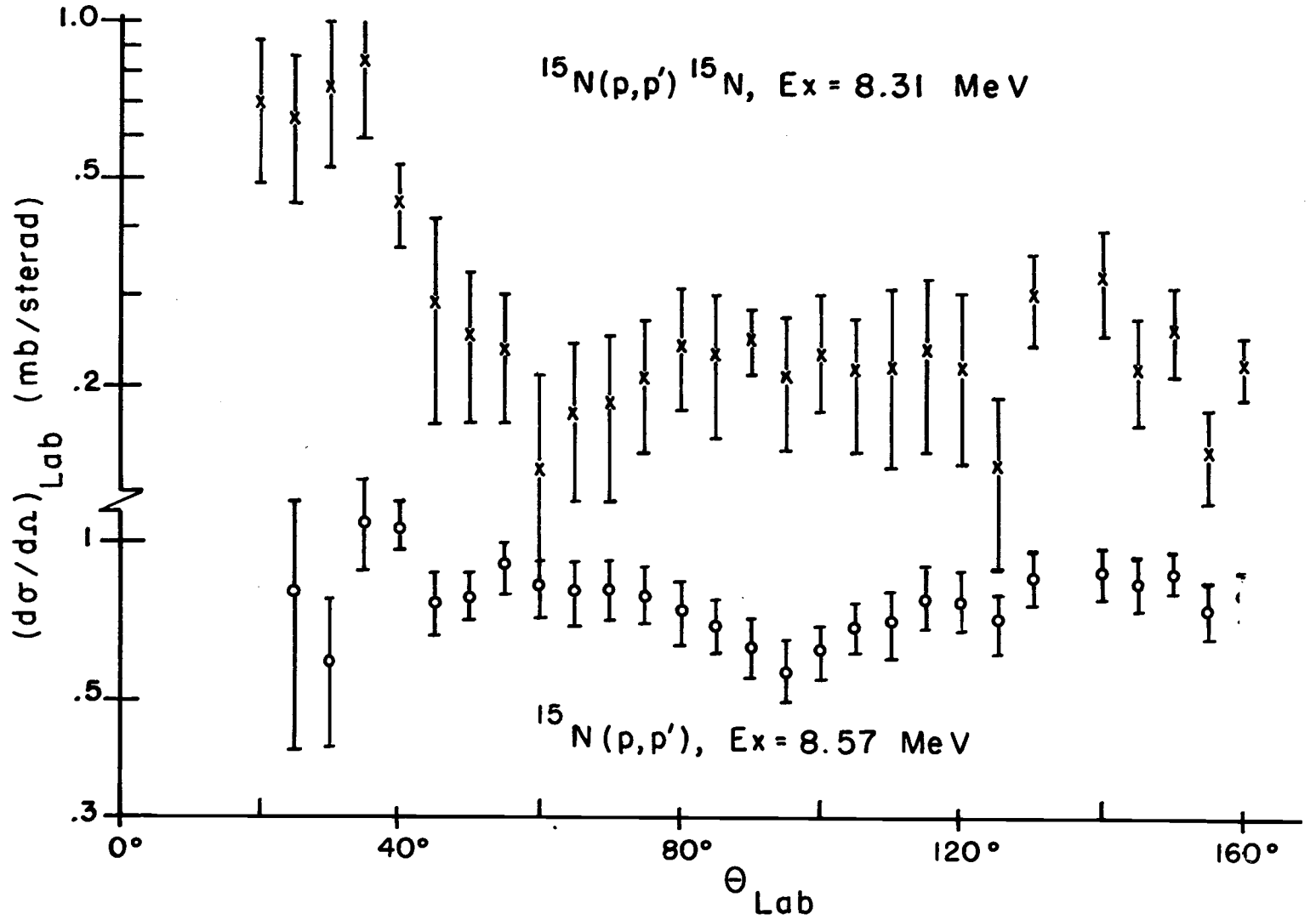

Figure 18. Angular distributions for the 8.31- and 8.57-MeV states of ^{15}N.

Excited States of ^{14}N

Nine states and doublets were resolved well enough to yield experimental cross sections over a large angular range. Experimental angular distributions are shown for the 2.3-MeV state (Figure 19), the 3.9-MeV state (Figure 20), the doublets at 5 and at 5.7 MeV (Figure 24), the 6.2-MeV state (Figure 23), the 6.4-MeV state and the 7.0-MeV state (Figure 22), and for the doublets at 8 MeV (Figure 23) and at 8.5 MeV (Figure 24). The error bars include uncertainties due to statistics, background subtraction, and a possible 6% error in absolute normalization.

4CC calculations were done in which the ground, 2.3-MeV, and 3.9-MeV states of ^{14}N were coupled with the ground state of ^{14}O. Three separate calculations were performed: a 4CC calculation, a 4CC calculation without a tensor force (4CC-no tensor), and a 4CC calculation including the derivative form factor (4CC-derivative). The last calculation was done in an effort to understand the meaning of the derivative form factor. Inspection of the target nucleus wave functions shows a peak at about the same radius as in the ^{15}N case, so the same values of R (2.4 fm) and A (0.5 fm) were used in the mass 14 4CC-derivative calculation as in the mass 15 case.

Figure 19 shows that the 4CC calculation for the 2.3-MeV state is of the correct magnitude (normalization factor of 1.0). The shape

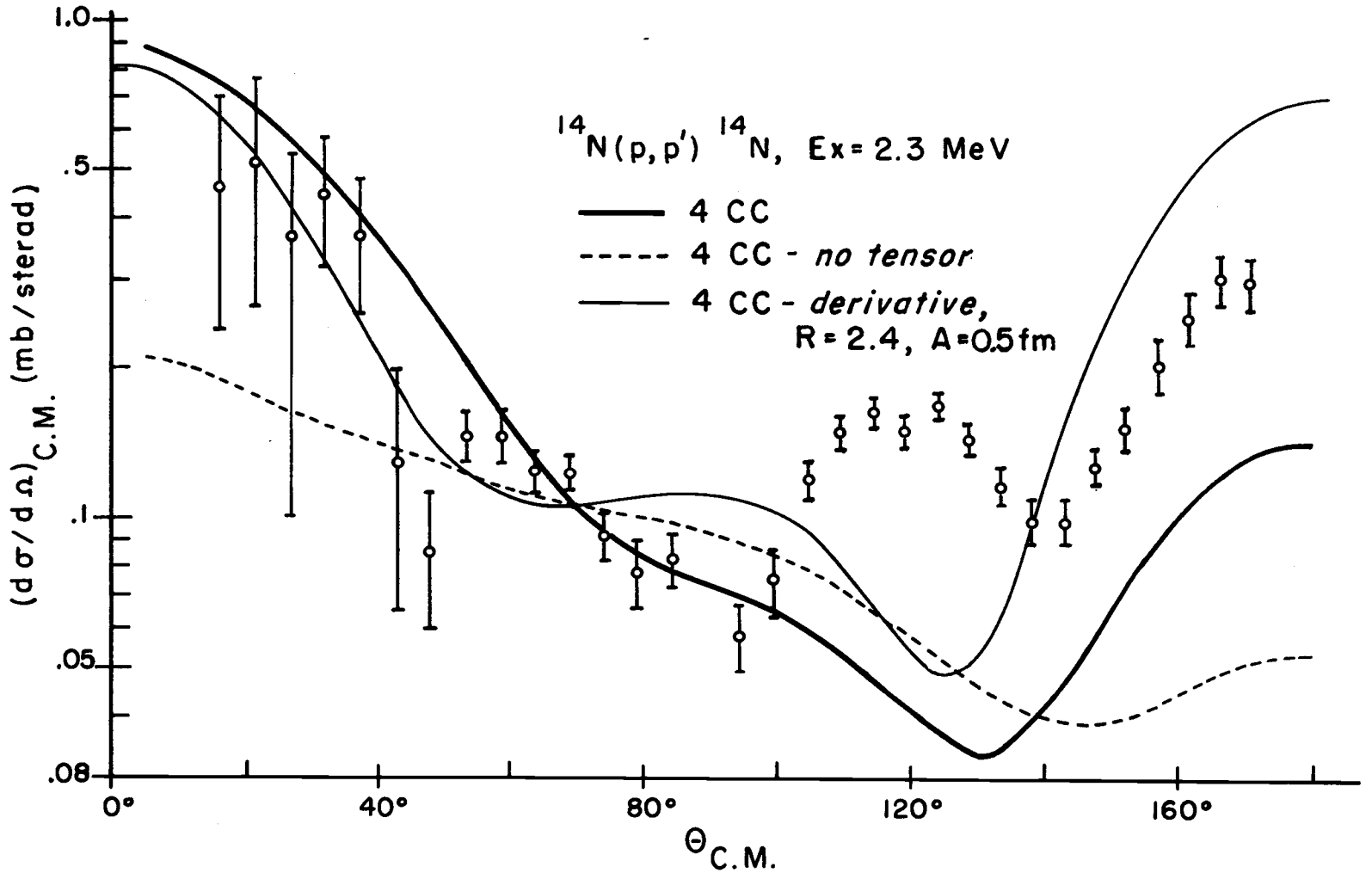

Figure 19. Angular distribution for the 2.3-MeV state of ^{14}N and comparison with the theory. Abbreviations used are defined in the text.

of the curve agrees with the data except for the peak near 120°. A similar peak in the experimental angular distribution is observed by Crawley et al. (12) for E_p = 24.8 MeV. They use the same microscopic model as in the present work, but incorporate it into a DWBA calculation, rather than a coupled channels calculation. The same Visscher-Ferrell wave functions were used for both analyses. They also find a dip in the theoretical cross section at 130°. Hence the dip seems to be either a result of the wave functions or of the microscopic model. The value of the tensor force strength which they obtained (3.9 MeV) agrees well with the one used here (4.0 MeV).

The 4CC-no tensor calculation (Figure 19) is clearly worse than the 4CC calculation in both shape and magnitude (normalization factor of 3.14). The 4CC-derivative calculation seems no better or worse than the 4CC calculation.

Figure 20 shows the results for the 3.9-MeV state. The tensor force is not expected to be important for this state. (It can be excited directly from the ground state through the V_{00} term of the microscopic potential, but only through a two-step process using an intermediate state (e.g., the 2.3-MeV state) through the tensor term.) This is born out by the fact that neither the shapes nor the magnitudes of the 4CC and 4CC-no tensor calculations differ by very much. The normalization factor for the 4CC calculation was 4.2. This is similar to the value found (6.8) by Curtis et al. (14). They used a DWBA

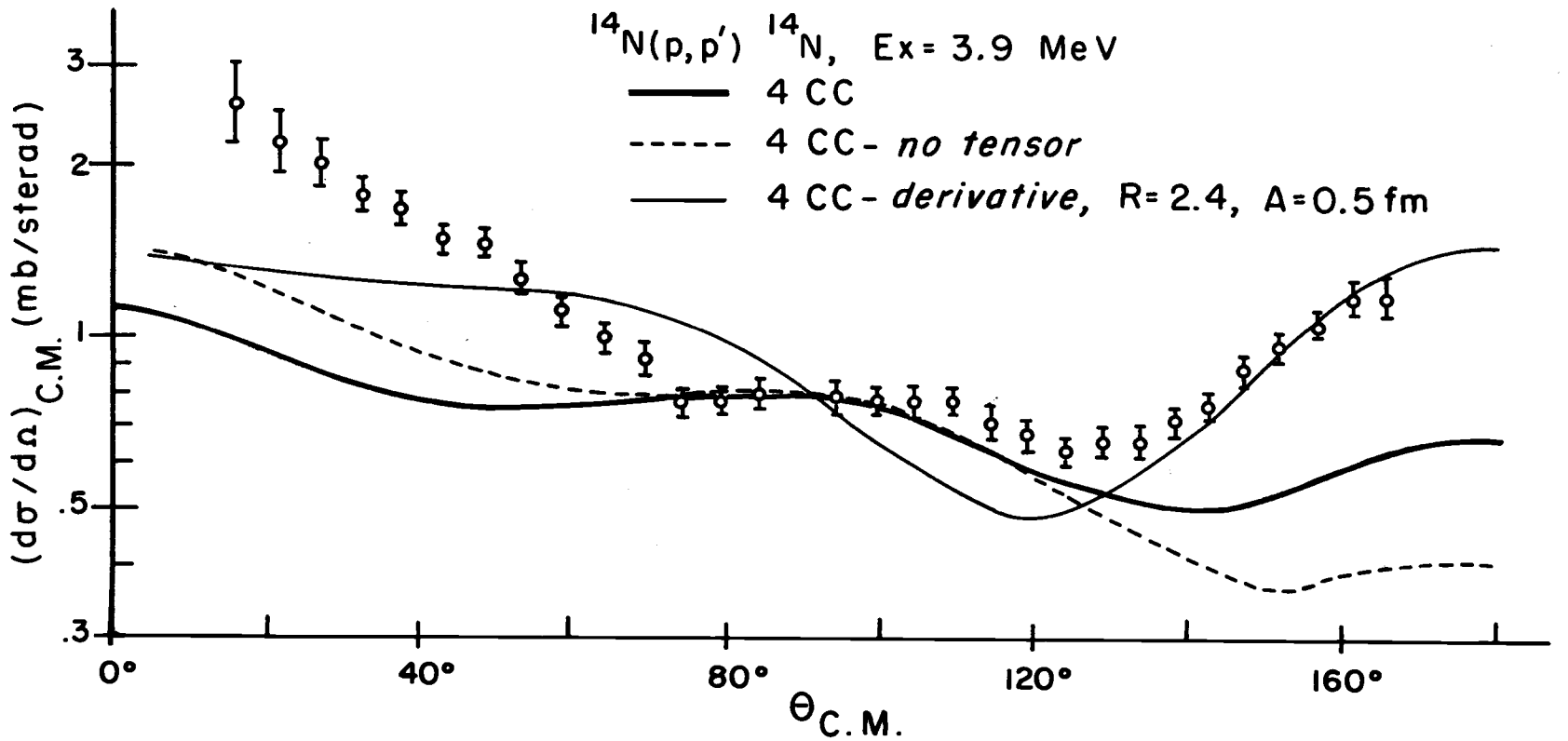

Figure 20. Angular distribution for the 3.9-MeV state of ^{14}N and comparison with the theory. Abbreviations used are defined in the text.

calculation and the microscopic model of the present work. The incoming proton energy was 14.5 MeV. Wave functions of Freed and Ostrander were used (16). (Although the general quality of fits to the data was not very good, a value of 3.9 MeV for the tensor force strength seemed to be indicated in fits to the 2.3-MeV state (14).)

Referring again to Figure 20, the 4CC-derivative calculation seems to be slightly better than the 4CC calculation.

Figure 21 shows the fits to the ^{14}O ground state. The data are that of Anderson and Wong as quoted by Richter and Parish (39). The data are for $E_p = 12.2$ MeV, and it may not be meaningful to compare with the present 17.2 MeV calculations. However, the 4CC-no tensor calculation seems worse, while the 4CC-derivative calculation is slightly better than the 4CC calculation.

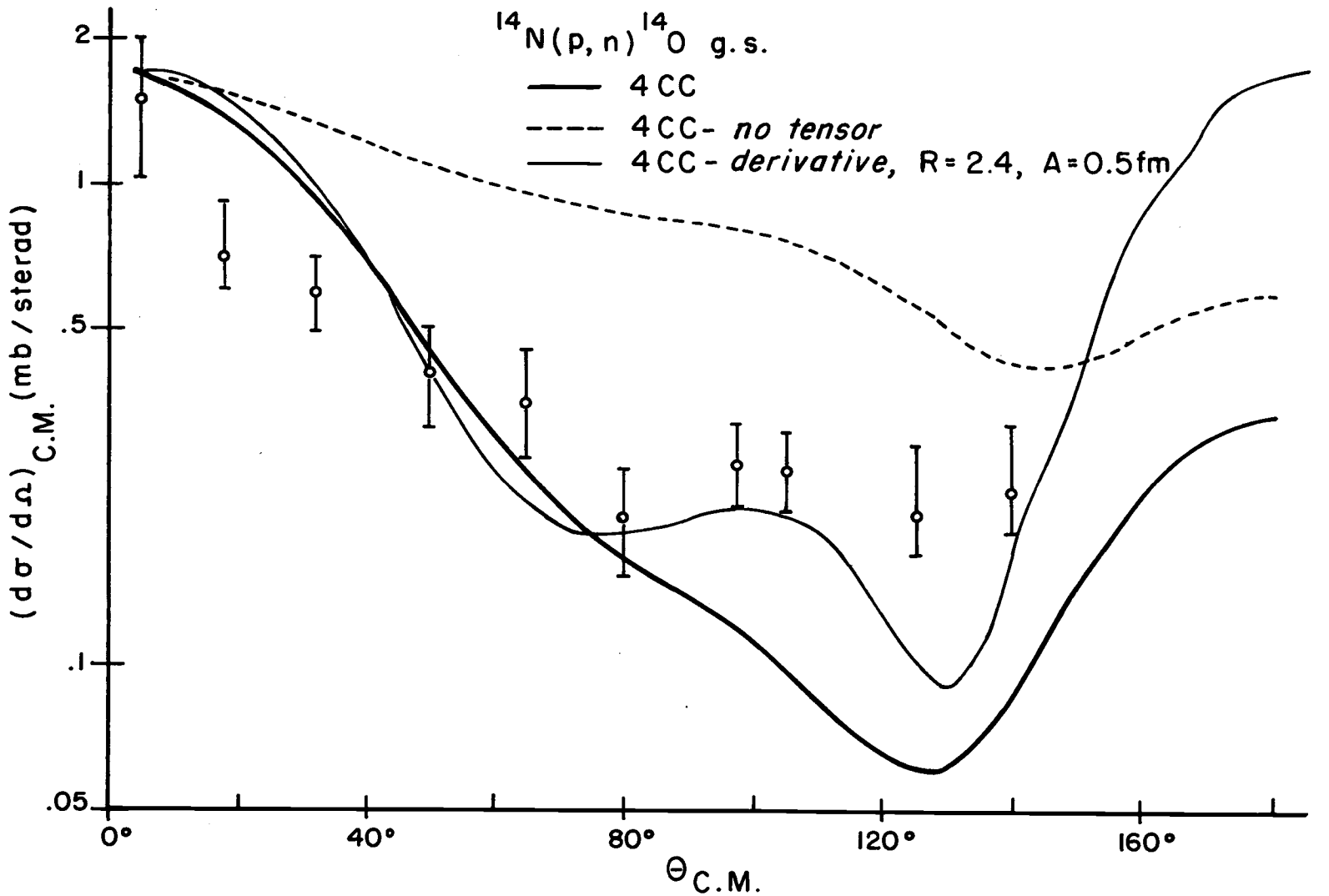

Figure 21. $^{14}N(p,n)^{14}O$, ground state, angular distribution and comparison with the theory. The data are from reference (39) for E_p = 12.2 MeV. Abbreviations used are defined in the text.

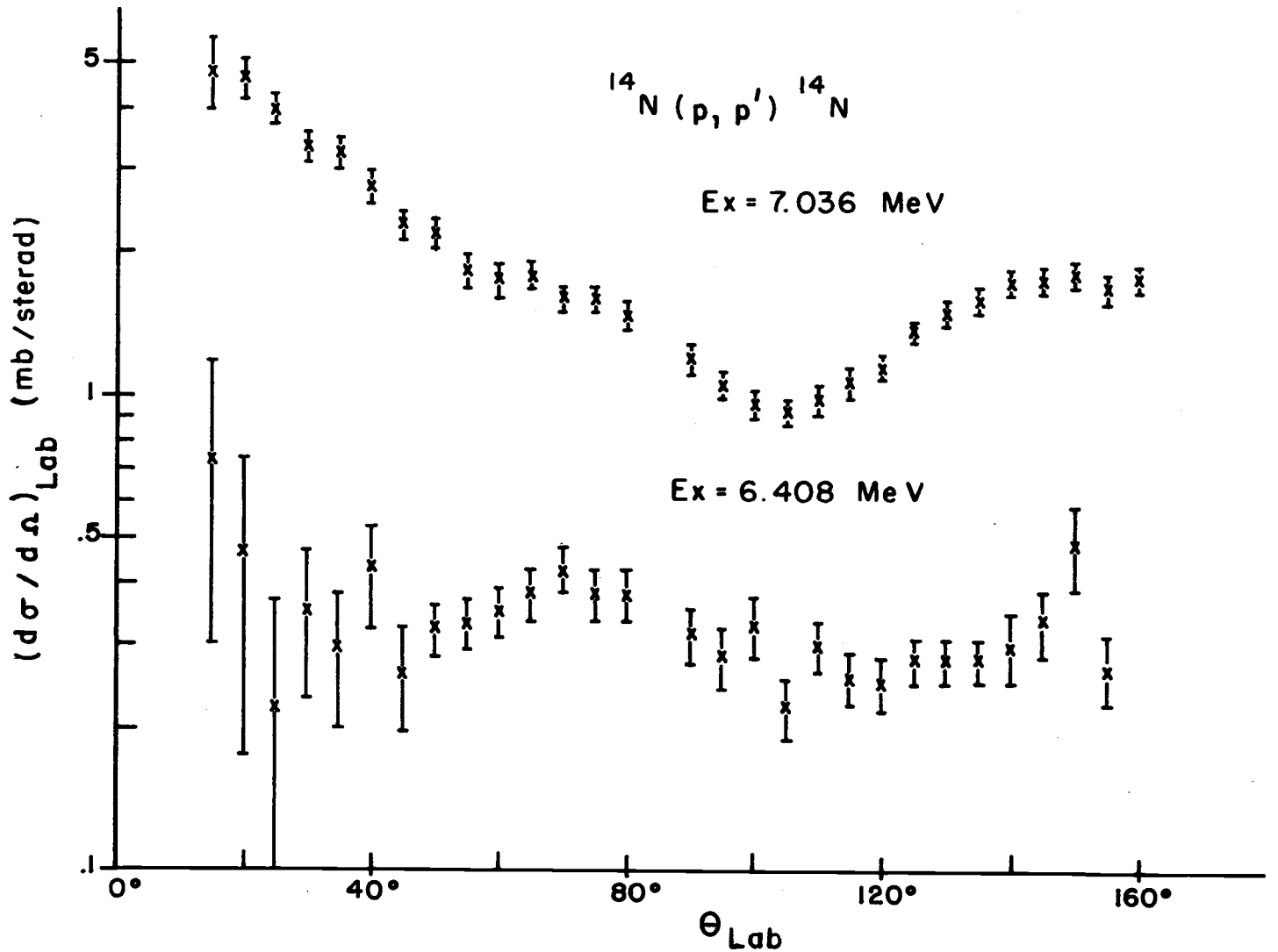

Figure 22. Angular distributions for the 6.4- and 7.0-MeV states of ^{14}N.

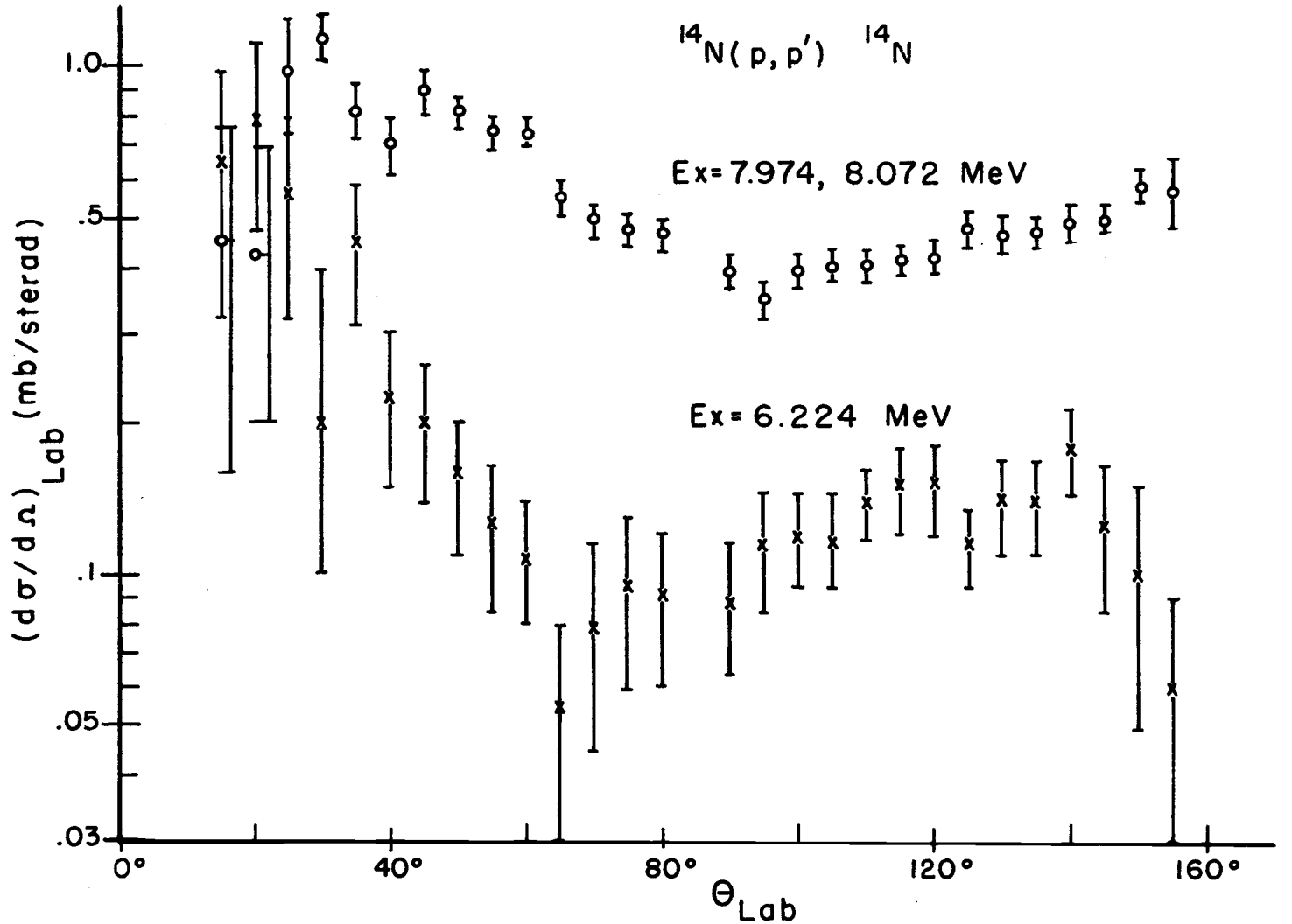

Figure 23. Angular distributions for the 6.2-MeV state and the 8-MeV doublet of ^{14}N.

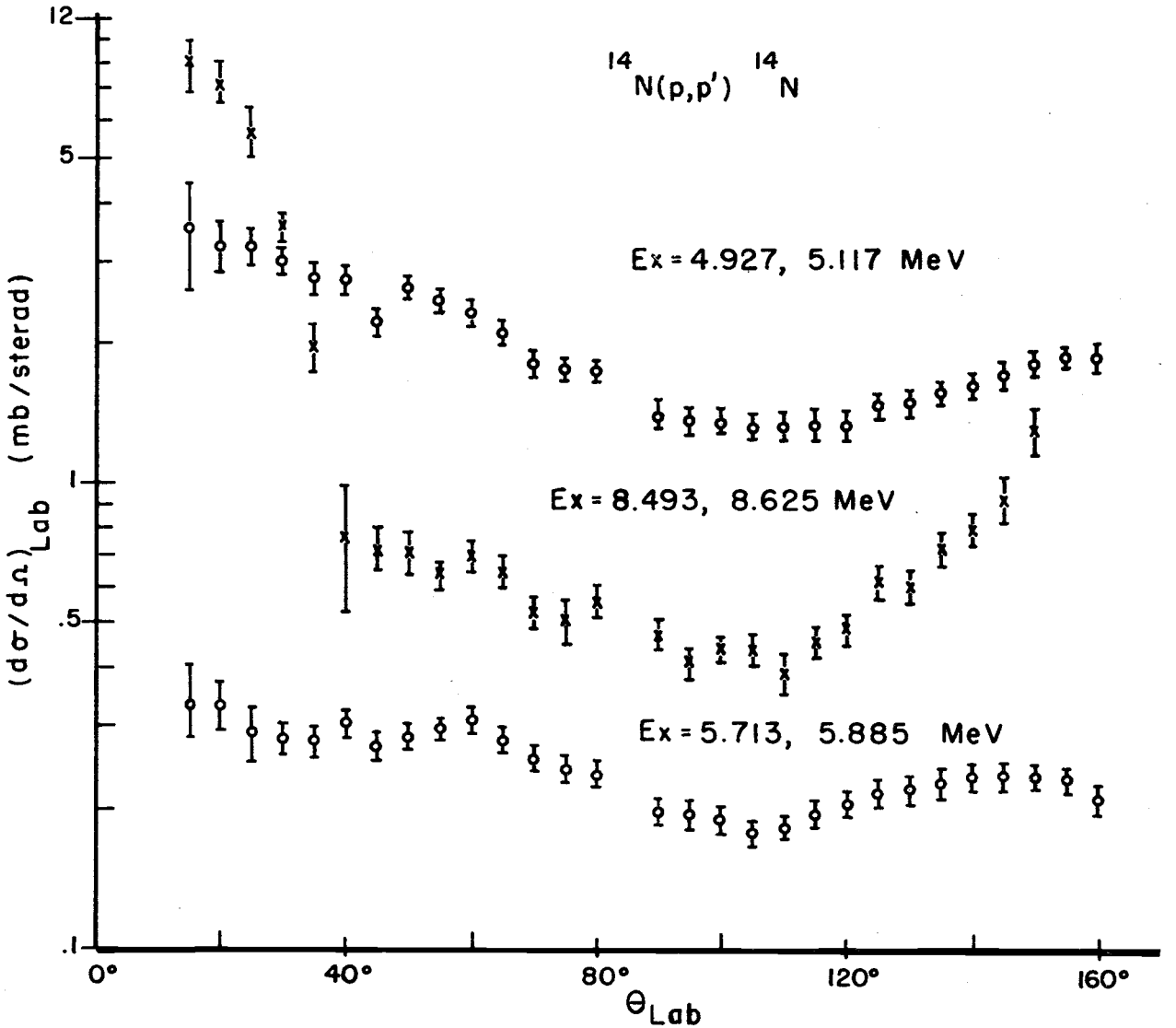

Figure 24. Angular distributions for the 5.0-, 5.8-, and 8.5-MeV doublets of ^{14}N.

V. CONCLUSION

There is clear evidence in both the mass 14 and the mass 15 systems for the need of a tensor force. The magnitude used (4.0 MeV) seems correct in that it results in reasonable fits to the data of this work, and is the same found by other workers at both higher and lower energies than the present work.

The microscopic model as incorporated by the coupled channel calculation gives reasonable fits to the data for the values of the potentials used. A persistent deficiency of the calculation seems to result in a dip at 130°-140°. This dip appeared in the calculations to several of the states and does not correspond to the data.

The calculations of the present work do not include the Pauli exclusion principle. A derivative form factor was introduced to simulate the effect of the Pauli principle. It is not clear why the inclusion of the derivative form factor worsened the fits for the 4CC calculation in mass 15, but gave perhaps a slight improvement in mass 14. Certainly in the 2CC calculation for ^{15}N the form factor greatly improved the fits; it may be similar to including exchange effects. Further study of this question is in progress.

Coulomb excitation was also neglected in the calculations. Comparison of the (p, n) and the (p, p') results shows that the (p, n) fits to the data are better. This suggests that coulomb excitation may be

important. An attempt to include the effect of coulomb excitation in a 2CC calculation for ^{15}N produced results similar to those obtained by using a longer range in the microscopic potential (a = 0.5, Figure 12), except that the forward peak was more pronounced. (Note that the inflection at 20° in the theoretical curve may also be present in the data.) The indication is that properly including coulomb excitation would improve the (p, p') fits at forward angles.

The weak-coupling model seems adequately to represent the 7.56-MeV and 5.27-MeV states of ^{15}N as a $p_{1/2}$ proton hole coupled to the 6.13-MeV state of ^{16}O. The data is also consistent with the model for the 7.30-MeV and 5.30-MeV states of ^{15}N as a $p_{1/2}$ proton hole coupled to the 7.12-MeV state of ^{16}O.

The 6.32-MeV, $3/2^-$ state of ^{15}N does not seem to be related to the 6.92-MeV, 2^+ state of ^{16}O by the simple weak-coupling model. There may be a small collective component in the 6.32-MeV state as evidenced by the slight improvement in shape for the fits to the data by the inclusion of the maximum collective enhancement indicated by the electromagnetic transition rates. Finally, the data of the present work are consistent with the interpretation of the upper $3/2^-$ level at 9.16 MeV as a largely collective state related to the 6.92-MeV state of ^{16}O by the weak-coupling model.

BIBLIOGRAPHY

1. Ajzenberg-Selove, F. and T. Lauritsen. Energy levels of light nuclei. VI. Nuclear Physics 11:1-340. 1959.

2. Alford, W.P., and K.H. Purser. Structure of low-lying states in A = 15 nuclei. Nuclear Physics A132:86-96. 1969.

3. Amos, K.A., V.A. Madsen, and I.E. McCarthy. Antisymmetrized distorted-wave approximation for nucleon-nucleus scattering. Nuclear Physics A94:103-128. 1967.

4. Anderson, J.D., S.D. Bloom, C. Wong, W.F. Hornyak, and V.A. Madsen. Effective two-body force inferred from the (p, n) reaction on ^{17}O, ^{18}O, ^{27}Al, and other light nuclei. Physical Review 177:1416-1435. 1969.

5. Atkinson, J., and V.A. Madsen. Effect of the knockout-exchange mechanism in nucleon-nucleus scattering. Physical Review 1:1377-1400. 1970.

6. Atkinson, J., and V.A. Madsen. Properties of the knockout-exchange amplitudes in nucleon-nucleus scattering. Physical Review Letters 21:295-297. 1968.

7. Ball, G.C., and J. Cerny. Microscopic analysis of the (^{3}He, t) and (^{3}He, $^{3}He'$) reactions on 1p-shell nuclei. Physical Review 177:1466-1497. 1969.

8. Beer, G.A., P. Brix, H.-G. Clerc, and B. Laube. Ground state electromagnetic widths of the 6.32 MeV level in ^{15}N. Physics Letters 26B:506-507. 1968.

9. Blair, J.S. Inelastic diffraction scattering. Physical Review 115:928-938. 1959.

10. Bussiere, A., N.K. Glendenning, B.G. Harvey, J. Mahoney, J.R. Meriwether, and D.J. Horen. Octupole states in ^{15}N and ^{15}O. Physics Letters 16:296-297. 1965.

11. Critchfield, C.L., and D.C. Dodder. On the scattering of protons in hydrogen. Physical Review 75:419-425. 1949.

12. Crawley, G.M., S.M. Austin, W. Benenson, V.A. Madsen, F.A. Schmittroth, and M.J. Stomp. Evidence for a tensor effective two-body interaction in the $^{14}N(p, p')$ 2.31 MeV excitation. Physics Letters 32B:92-94. 1970.

13. Crawley, G.M., and G.T. Garvey. Inelastic scattering in the 2s--1d shell. I. Even-A nuclei. Physical Review 160:981-996. 1967.

14. Curtis, T.H., H.F. Lutz, D.W. Heikkinen, and W. Bartolini. Proton induced reactions on mass-14 nuclei. To be published in Nuclear Physics.

15. Daehnick, W.W., and R. Sherr. Energy dependence of elastic and inelastic scattering from ^{12}C for protons between 14 and 19 MeV. Physical Review 133:B934-B947. 1964.

16. Freed, N., and P. Ostrander. Velocity-dependent interactions in mass-14 nuclei. Nuclear Physics A111:63-80. 1968.

17. Gill, R.D., J.S Lopes, O. Häusser, and H.J. Rose. Lifetime measurements in mass-15 nuclei. Nuclear Physics A121:209-223. 1968.

18. Gill, R.D., J.S. Lopes, B.C. Robertson, R.A.I. Bell and H.J. Rose. A study of positive-parity states in ^{15}O. Nuclear Physics A106:678-688. 1968.

19. Halbert, E.C., and J.B. French. Shell model for the positive-parity states of ^{15}N. Physical Review 105:1563-1569. 1957.

20. Harvey, B.G., J.R. Meriwether, J. Mahoney, A. Bussiere de Nercy, and D.J. Horen. Scattering of 40.5 MeV alpha particles by ^{12}C, ^{13}C, ^{14}N, ^{15}N, ^{16}O, and ^{18}O. Physical Review 146:712-722. 1966.

21. Häusser, O., R.D. Gill, J.S. Lopes, and H.J. Rose. Gamma rays from positive parity states in ^{15}N. Nuclear Physics 84:683-694. 1966.

22. Häusser, O., H.J. Rose, J.S. Lopes, and R.D. Gill. Comparison of signs of mixing ratios to model predictions. Physics Letters 22:604-606. 1966.

23. Hiebert, J.C., E. Newman, ane R.H. Bassel. Distorted-wave born-approximation analysis of the (d, ^{3}He) reaction of "closed shell" nuclei. Physical Review 154:898-920. 1967.

24. Holbrow, C.H., R. Middleton, and W. Focht. Study of ^{14}N by several transfer reactions. Physical Review 183:880-887. 1969.

25. Kallio, A., and K. Kolltveit. An application of the separation method in shell-model calculations. Nuclear Physics 53:87-96. 1964.

26. Kutschera, W., D. Schwahn, and B. Poyh. Ground-state transition of the 7.28 MeV state in ^{15}O. Nuclear Physics A124:693-695. 1969.

27. Lane, A.M. Reduced widths of individual nuclear energy levels. Reviews of Modern Physics 32:519-566. 1960.

28. Lopes, J.S., O. Häusser, H.J. Rose, A.R. Poletti, and M.F. Thomas. The 3/2 → 1/2 hole transitions in mass 15. Nuclear Physics 76:223-231. 1966.

29. Madsen, V.A. A Formalism for direct inelastic scattering and charge exchange. Nuclear Physics 80:177-197. 1966.

30. Mollenauer, J. General purpose gas target system. The Review of Scientific Instruments 36:1044. 1965.

31. Mubarakmand, S., and B.E.F. Macefield. Parities of states in ^{15}O and ^{33}Cl. Nuclear Physics A98:82-96. 1967.

32. Murry, K.M., and J.C. Ritter. $^{16}O(\gamma, n)^{15}O^{*}$ and $^{16}O(\gamma, p)^{15}N^{*}$ reactions and the electromagnetic decay of $^{15}O^{*}$ and $^{15}N^{*}$. Physical Review 182:1097-1103. 1969.

33. Negele, J.W. Structure of finite nuclei in the local density approximation. Doctoral thesis. Ithaca, N.Y., Cornell University, 1969. 230 numb. leaves.

34. Peele, R.E. Differential cross sections for the scattering of medium energy protons on carbon. Physical Review 195:1311-1323. 1957.

35. Perey, F. G. Optical-model analysis of proton elastic scattering in the range of 9 to 22 MeV. Physical Review 131:745-763. 1963.

36. Petrovich, F., H. McManus, V. A. Madsen, and J. Atkinson. Finite-nucleus G matrix in the microscopic description of inelastic proton scattering. Physical Review Letters 22:895-899. 1969.

37. Phillips, G. W., and W. W. Jacobs. Structure of ^{15}N and the $^{14}N(d, p)^{15}N$ reaction. Physical Review 184:1052-1060. 1969.

38. Phillips, G. W., F. C. Young, and J. B. Marion. Energy levels and electromagnetic transitions in ^{15}N from the $^{13}C(^{3}He, p\gamma)^{15}N$ reaction. Physical Review 159:891-908. 1967.

39. Richter, A., and L. J. Parish. Compound-nucleus effects in (p, n) charge-exchange reactions on light nuclei. Physical Review 21:1824-1828. 1968.

40. Rose, H. J., O. Häusser, and E. K. Warburton. Evidence for a nuclear tensor force from mass-14 beta- and gamma-ray data. Reviews of Modern Physics 40:591-610. 1968.

41. Rose, J. J., and J. S. Lopes. Collective retardation in mass 15 nuclei. Physics Letters 18:130-131. 1965.

42. Rose, H. J., and J. S. Lopes. The $3/2^{-} \rightarrow 1/2^{-}$ mirror transitions in mass 15. Physics Letters 22:601-603. 1966.

43. Rose, H. J., J. S. Lopes, and W. Greiner. Destructive interference of hole and collective E2 transition amplitudes. Physics Letters 19:686-689. 1966.

44. Satchler, G. R. The distorted-waves theory of direct nuclear reactions with spin-orbit effects. Nuclear Physics 55:1-33. 1964.

45. Schiffer, J. P., G. C. Morrison, R. H. Siemssen, and B. Zeidman. Study of the (d, p) reaction in the 1 p shell. Physical Review 164:1274-1284. 1967.

46. Schmittroth, F. A. A comparison of effective interactions in nuclear structure and scattering. Doctoral thesis. Corvallis, Oregon State University, 1969. 140 numb. leaves.

47. Sherr, R., J. B. Gerhart, H. Horie, and W. F. Hornyak. Decay rates of ^{14}C, $^{14}N^*$, and ^{14}O. Physical Review 100:945-946. 1955.

48. Shukla, A. P., and G. E. Brown. Core polarization effects in ^{15}O and ^{15}N. Nuclear Physics A112:296-328. 1968.

49. Siefkin, H. E., P. M. Cockburn, and R. W. Krone. Levels in ^{15}N resulting from the proton capture of ^{14}C. Nuclear Physics A128:162-182. 1969.

50. Silverstein, E. A. Calculation of the G factor for gas scattering experiments. Nuclear Instruments and Methods 4:53-66. 1959.

51. Smythe, R. Relativistic equations and tables for ion energy determination by crossover technique. The Review of Scientific Instruments 35:1197-1200. 1964.

52. Snelgrove, J. L. Energy dependence and spectroscopy in the $^{16}O(p, d)^{15}O$ and $^{15}N(p, d)^{14}N$ reaction. Doctoral Thesis. East Lansing, Michigan State University, 1968. 181 numb. leaves.

53. Stomp, M. To be published.

54. Tamura, T. Analyses of the scattering of nuclear particles by collective nuclei in terms of the coupled-channel calculation. Reviews of Modern Physics 37:679-708. 1965.

55. Visscher, W. M., and R. A. Ferrell. Beta decay of ^{14}C and nuclear forces. Physical Review 107:781-796. 1967.

56. Warburton, E. K., and J. W. Olness. Angular correlations in the $^{13}C(He^3, p\gamma)^{15}N$ reaction: levels of ^{15}N. Physical Review 147:798-709. 1966.

57. Warburton, E. K., J. W. Olness, and D. E. Alburger. Studies of electromagnetic transitions in ^{15}N and ^{15}O. Physical Review 140:B1202-1236. 1965.

58. Warburton, E. K., P. D. Parker, and P. F. Donovan. Location of the p-shell hole states in mass 15 nuclei. Physics Letters 19:397-398. 1965.

59. Wong, C., J.D. Anderson, V.A. Madsen, F.A. Schmittroth, and M.J. Stomp. Polarization and the angular distribution of neutrons from the $^{14}C(p,n)$ reaction and the tensor force. To be published.

60. Wong, C., J.D. Anderson, J. McClure, B. Pohl, V.A. Madsen, and F. Schmittroth. $^{14}C(p,n)^{14}N$ reaction and the two-body force. Physical Review 160:769-774. 1967.